Deep–Sea Research Part I 122 (2017) 1–16

Contents lists available at ScienceDirect

Deep–Sea Research I

journal homepage: www.elsevier.com/locate/dsri

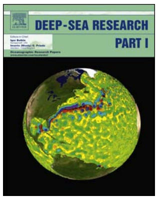

The influence of Gulf Stream eddies and meanders on near-surface chlorophyll

Peter Gaube*,[1], Dennis J. McGillicuddy Jr.,

Department of Applied Ocean Physics and Engineering, Woods Hole Oceanographic Institution, Woods Hole, MA 02543, USA

ABSTRACT

The Gulf Stream region contains strong mesoscale variability that significantly influences planktonic ecosystems residing therein. Meanders of the Gulf Stream can be identified as eastward propagating features in maps of sea level anomaly. These meanders can become unstable and pinch off to form nonlinear mesoscale eddies (rings) that trap large parcels of water. Following formation, ecosystems trapped within these eddies are subjected to temporally varying vertical velocities throughout their lifetime. As a result of both horizontal advection and vertical fluxes, multiple physical-biological mechanisms can simultaneously influence phytoplankton communities trapped in eddies. In this study we examine how the near-surface chlorophyll field (CHL) evolves in meanders and eddies by comparing satellite observations with an eddy-resolving ocean model.

Prior *in situ* and satellite observations have revealed that during the formation of cyclonic Gulf Stream meanders, water with elevated CHL is transported southward. In anticyclonic meanders, water with reduced CHL is transported northward. Alternating submesoscale patches of upwelling and downwelling occur along the meandering front; however, evidence of a biological response to meander-induced vertical motion was not observed in meander-centric composite averages. During the formation of nonlinear Gulf Stream eddies, elevated and suppressed CHL is trapped and subsequently transported westward in cyclones and anticyclones, respectively. Following formation, CHL is observed to increase in the cores of anticyclones. The observed positive trend in CHL in anticyclones is consistent with the influence of eddy-induced Ekman pumping (eddy/wind interaction) that generates upwelling in anticyclones and downwelling in cyclones.

To substantiate the influence of eddy-induced Ekman pumping on CHL in Gulf Stream eddies, two separate eddy-resolving physical-biological simulations are compared. The first simulation is forced with a realistic surface stress that includes the influence of ocean surface currents. The second simulation neglects this process. The time evolution of CHL within eddies is very different in these two simulations. The model that includes eddy-induced Ekman pumping generates temporal trends in CHL that are similar to the observations.

1. Introduction

Gulf Stream (GS) meanders and eddies are highly energetic features that influence ecosystem dynamics across multiple trophic levels (Davis and Wiebe, 1985; Olson and Backus, 1985; Boyd et al., 1986; Ducklow, 1986; Craddock et al., 1992; Pascual et al., 2015). Eddies and meanders in this region of the North Atlantic are amongst some of the most energetic coherent mesoscale structures on earth, with sea level anomalies representing the upper 90th percentile in amplitude globally, as documented by Chelton et al. (2011b).

Prior observations of GS eddies, or rings, found that cyclonic cold-core rings trap Slope water from north of the GS during formation (Pingree et al., 1979; The Ring Group, 1981). On the other hand, anticyclonic warm-core rings trap and transport water with relatively low phytoplankton concentration from the Sargasso Sea northwestward towards the continent (Joyce, 1985; Smith and Baker, 1985; Olson, 1986; Ryan et al., 2001). These warm-core anticyclonic rings are characterized by a nutrient-depleted surface layer (Fox et al., 1984; Franks et al., 1986; Nelson et al., 1989) and have also been observed to advect CHL around their periphery (García-Moliner and Yoder, 1994).

Coherent mesoscale structures (CMS) in the GS region, defined here as mesoscale eddies and meanders, generate large anomalies in sea level, surface temperature and ocean color. These characteristics made CMS in the GS region prime targets for some of the earliest published satellite observations [*e.g.*, Gordon et al., 1982]. A recent analysis of sea level anomalies (SLA) and near-surface chlorophyll concentration

---

* Corresponding author.
E-mail addresses: pgaube@whoi.edu, pgaube@apl.washington.edu (P. Gaube).
[1] Current Affiliation: Air-Sea Interaction and Remote Sensing Department, Applied Physics Laboratory, University of Washington, Seattle, WA 98105, USA.

http://dx.doi.org/10.1016/j.dsr.2017.02.006
Received 14 August 2015; Received in revised form 7 February 2017; Accepted 12 February 2017

(CHL), concluded that multiple mechanisms influence the CHL signatures of GS eddies, including the trapping of phytoplankton in eddy interiors and a CHL response to the upwelling of nutrients during the intensification of cyclones (Gaube et al., 2014). Given the diversity of processes involved, it is not clear *a priori* whether a coherent biological response should emerge in meander- and eddy-centric composite averages of CHL.

Previous studies of physical/biological interaction in Gulf Stream eddies and meanders were focused on the synoptic view from "snapshots" of individual CMS. This study presents a meander- and eddy-centric composite analysis – to elucidate the mean response of the CHL field to these perturbations. We use satellite observations of GS eddies and meanders in conjunction with an eddy-resolving, coupled physical/biological model to investigate the spatial/temporal variability of CHL in CMS by constructing composite averages from hundreds of weekly realizations of eddies and meanders (realizations are defined here as a single "snapshot" of a CMS). The temporal evolution of CHL following eddy and meander formation is of particular interest because mechanisms affecting CHL in CMS that are undergoing formation and/or intensification are different from those that are decaying, resulting in distinct temporal trends in CHL (Gaube et al., 2014). The GS region is characterized by negative cross correlation between sea level and CHL anomalies (Gaube et al., 2014) which is consistent with the trapping of CHL and the enhancement (reduction) of CHL during the formation and intensification of cyclones (anticyclones). However, it is important to note that other processes are also active (*e.g.,* eddy-induced Ekman pumping, meander-induced vertical motion), thus analysis of cross correlation alone is not sufficient to differentiate among the various mechanisms of mesoscale physical/biological interaction on CHL.

In the study presented here, we use a model that reproduces the observed negative correlation in the GS region to evaluate the relative importance of these various mechanisms in determining mesoscale CHL anomalies. The manuscript is organized as follows: In Section 2 we provide a brief overview of mesoscale physical/biological mechanisms. Section 3 describes the data sets analyzed and methods used to identify and track CMS and construct CMS-centric composite averages and composite average time series. Section 4 describes the simulated and observed regional-scale variations in sea level and CHL. The influence of eddies and meanders on CHL as inferred from satellite observation and a numerical simulation is described in Sections 5 and 6. A summary and the conclusions of this study are presented in Section 7.

2. Mechanisms of physical/biological interaction in Gulf Stream eddies and meanders

For the purpose of this study, the influence of eddies on CHL will be segregated into processes that advect phytoplankton, either horizontally or vertically, those that affect nutrient supply, and those that modulate phytoplankton light exposure within the euphotic zone.

Mesoscale modulations in phytoplankton light exposure (*i.e.,* changes in mixing layer depth within CMS) have been shown to be important in regions where primary production is limited by light, rather than nutrients (Lévy et al., 1998, 1999). In addition, seasonal modulation of stratification can result in eddy-induced perturbations of CHL that are different in the summer and winter (*e.g.* CHL perturbations in the South Indian Ocean are dominated by stirring in the summer and by eddy-induced Ekman pumping and/or entrainment in the winter; Gaube et al., 2013; Dufois et al., 2014). In this study, our choice not to address seasonal variability is motivated in part by an earlier analysis indicating the structure of CMS-centric composite averaged CHL anomalies does not vary substantially throughout the year (Gaube, 2012). In addition, a number of observations of individual eddies revealed that changes in mixed layer depth were not time-synchronous with CMS lifetimes and neither observed nor simulated eddies and meanders were preferentially generated in any particular season.

The horizontal advection of nutrients and phytoplankton can be broken down into two mechanisms: stirring, which occurs primarily around the peripheries of eddies and meanders, and trapping and subsequent transport in the interiors of eddies. Upwelling and downwelling in eddies and meanders can also be segregated into vertical velocities resulting from the displacement of isopycnals generated by internal synoptic dynamics (*e.g.,* meander-induced vertical velocities, eddy-pumping, or eddy/eddy interaction) and those that are the result of a forced response (*e.g.,* eddy-induced Ekman pumping). These mechanisms are reviewed briefly here.

The azimuthal advection (transport of water by rotational currents) of phytoplankton around the peripheries of eddies and meanders (referred to here as eddy stirring) has been shown to be the dominant mechanism, in a globally-averaged sense, by which eddies influence CHL in the midlatitudes on time scales on the order of weeks to months and spatial scales larger than 2° (Chelton et al., 2011a) . Eddy stirring results in composite CHL anomalies (averages of hundreds to thousands of realizations), that have spatial structure characterized as asymmetric dipoles with the sign and alignment of the dipoles being a function of the rotational sense of the eddy in relation to the direction of the ambient CHL field (Chelton et al., 2011a, see their Fig. 4 for a schematic of this process).

Nonlinear eddies, for which the rotational velocities of the eddy are faster than the eddy propagation speed, can trap fluid in their interiors (McWilliams and Flierl, 1979; Flierl, 1981). Ecosystems trapped in eddies during formation act to "prime" the eddy interior towards either elevated or suppressed phytoplankton concentration (for a schematic of this process see Fig. 3 of McGillicuddy (2016)). As discussed in Section 1, anticyclonic GS eddies trap Sargasso Sea water that is low in phytoplankton, CHL, and nutrients while cyclonic GS eddies trap Slope water that is high in phytoplankton, CHL and nutrients. The expected temporal evolution of CHL in trapped ecosystems, assuming all other factors remain constant, is a step function that takes place at the time of eddy formation, resulting in negative (positive) CHL anomalies in GS anticyclones (cyclones) (Gaube et al., 2014).

Processes affecting CHL *via* the vertical flux of nutrients and CHL in CMS include: (1) Isopycnal displacement resulting from upwelling and downwelling associated with meandering of the GS; (2) the vertical displacement of isopycnals during eddy intensification and decay; and (3) eddy-induced Ekman pumping.

Meandering of the GS can lead to vertical motion by a variety of processes, including kinematic effects such as meander propagation as well as dynamical effects such as frontogenesis and frontolysis (Woods, 1988; Bower, 1991; Flierl and Davis, 1993; Olson et al., 1994; Spall and Richards, 2000; Lima et al., 2002). Such vertical motions are typically manifested as alternating patches of upwelling and downwelling oriented along the front (for a schematic of this process see Fig. 2 of Olson et al., 1994). However, the phase relationship between the upwelling and downwelling cells and their attendant CHL anomalies is complicated because of downstream advection. For example, positive CHL anomalies associated with upwelling can be advected downstream by the GS, and accumulate near the adjacent meander trough (Hitchcock et al., 1993; Olson et al., 1994; Lima et al., 2002). Similarly, negative CHL anomalies associated with downwelling may also be displaced by horizontal advection, as has been noted in other mesoscale (Lévy et al., 1999) and submesoscale (Lévy et al., 2001) fronts. Furthermore, GS meanders are not impermeable barriers to cross-front transport and the entrainment of water into meanders on their leading edge and the detrainment of water on their trailing edge (see Fig. 2 of Bower, 1991 for a schematic of this process) may act to dilute CHL anomalies associated with upwelling and downwelling in meanders. Given the diversity of processes involved, it is not clear *a priori* whether a coherent biological response should emerge in meander-centric composite averages of CHL—and this is one of the questions motivating the present study.

The intensification of cyclonic eddies results in the upward displacement of isopycnals and upwelling of nutrients, and if a deep chlorophyll maximum (DCM) is present, CHL into the euphotic zone. In this context, satellite observations alone are not sufficient to distinguish between a biological response to upwelled nutrients from simple uplift of the DCM (McGillicuddy et al., 2001). During the intensification of anticyclonic eddies, the downward displacement of isopycnals results in the downwelling of nutrients and CHL. Fluxes associated with eddy intensification are expected to generate composite CHL anomalies with spatial structure characterized as a monopole of positive or negative CHL anomaly in cyclones and anticyclones, respectively. The expected temporal evolution of CHL as a result of upwelling/downwelling during early life stages is expected to be positive in cyclones and negative in anticyclones with the greatest rate of change occurring during eddy intensification (Gaube et al., 2014). It is important to note that processes such as eddy-eddy interaction can generate vertical velocities resulting from changes in eddy amplitude. The CHL response to such transient vertical velocities are not time-synchronous with the lifetimes of eddies and as such are unlikely to be preserved in the composite-averaged time series investigated here.

Current-induced Ekman pumping is driven by rotating eddy surface currents that impart a curl on the surface stress from the relative motion between air and water (Dewar and Flierl, 1987; Gaube et al., 2015). This surface stress curl has a polarity opposite to that of the vorticity of the eddy, thus generating Ekman upwelling in the cores of anticyclones (Dewar and Flierl, 1987) and downwelling in the cores of cyclones (McGillicuddy et al., 2007; Gaube et al., 2015; McGillicuddy, 2015). This process is shown schematically for anticyclones in Fig. 7 of Martin and Richards (2001) and for cyclones in Fig. 3 of Olson et al. (2015). The expected CHL response to eddy-induced Ekman pumping is therefore opposite that expected from vertical fluxes associated with eddy intensification. Fluxes associated with eddy-induced Ekman pumping are expected to generate composite averaged CHL anomalies with spatial structure characterized as a monopole of positive and negative CHL anomalies in anticyclones and cyclones, respectively. Time series of CHL in eddies in which eddy-induced Ekman pumping is the primary mechanism influencing CHL are expected to be display a positive trend in anticyclones and a negative trend in cyclones (Gaube et al., 2014).

3. Methods

3.1. Satellite observations

The observed influence of CMS on CHL is investigated in satellite observations of sea surface height (SSH) and ocean color. The SSH fields analyzed here are the Reference Series constructed by merging Topex/Posiden, Jason-1 and Jason-2 measurements with ERS-1, −2 or ENVISAT (Ducet et al., 2000) and were downloaded from Collecte Localis Satellites (CLS/AVISO) at 7-day intervals on a 1/4° latitude by 1/4° longitude grid. Sea level anomaly fields (SLA) are defined as:

$$\mathrm{SLA} = \mathrm{SSH} - \langle \mathrm{SSH} \rangle, \tag{1}$$

where ⟨SSH⟩ denotes the low-pass filtered SSH fields smoothed using a loess filter with a half-power cutoff of 20° in longitude and 10° in latitude (all abbreviations used in this manuscript are summarized in Table 1). This spatial filter has been shown to effectively remove seasonal heating and cooling effects from the SSH field while retaining mesoscale variability (Chelton et al., 2007, 2011b).

Satellite-derived CHL is indicative of the biomass of primary producers. Phytoplankton intracellular chlorophyll concentrations are, however, highly variable because of physiological acclimations to light availability, temperature, nutrient limitation, and phytoplankton community composition (Laws and Bannister, 1980; Geider, 1987; Falkowski and LaRoche, 1991; Behrenfeld et al., 2008). This “plasticity” in chlorophyll to carbon ratio must therefore be considered when interpreting CHL variability in natural phytoplankton communities. However, in an earlier study of mesoscale variability in CHL and phytoplankton biomass, as derived from backscattering at 440 nm, suggest that CHL and phytoplankton carbon in eddies in the GS region covary in space and time (Gaube, 2012). In the study presented here we will therefore attribute mesoscale variations in CHL to fluctuations in biomass, thereby assuming that variations in the chlorophyll to carbon ratio are of secondary importance in this context.

Table 1
Overview of the abbreviations and variables.

Abbreviations	Definitions	Equations
CMS	Coherent Mesoscale Structure	
GS	Gulf Stream	
SSH	Sea Surface Height	1
ADT	Absolute Dynamic Topography	
MDT	Mean Dynamic Topography	
SLA	Sea Level Anomaly	1
L_s	Speed-Based Radius Scale	
CHL	Near-Surface Chlorophyll Concentration	2
$\sigma(CHL)$	Standard Deviation of CHL	
CHL'	CHL Anomaly	2
CHL''	Normalized CHL Anomaly	3
$\Delta CHL'$	Change in CHL' since CMS Detection	4
$\boldsymbol{\tau}$	Surface Stress	5,6

All satellite observations were interpolated to a common 1/4° latitude by 1/4° longitude grid at 5-day time steps. This time increment as chosen to match the 5-day averages archived from the model described in Section 3.3. The 5-day period common to the observations and model will henceforth be referred to as a “week”. Satellite observations were analyzed during the ~5.5-year time period January 2000 through July 2005 during which concurrent observations of SLA and CHL are available and equivalent in length to the final 5.5 years of the eddy-resolving simulation analyzed in this study.

Near-surface chlorophyll-a concentration (CHL) fields were estimated from measurements of ocean color made by the Sea-viewing Wide Field-of-view Sensor (SeaWiFS) sensor using the Garver-Siegel-Maritorena (GSM) semi-analytical ocean color algorithm (Garver and Siegel, 1997; Maritorena et al., 2002; Siegel et al., 2002). The CHL observations were filtered in space and time following the procedure outlined in Gaube et al. (2013). The daily averaged 9 km SeaWiFS CHL observations were $\log_{10}$ transformed and block averaged onto a 1/4° latitude by 1/4° longitude grid. These $\log_{10}$-transformed CHL fields were then filtered in time with a filter half-power cutoff of 35 d, commensurate with the temporal smoothing used in the AVISO SSH fields. This temporal smoothing aided in the filling of gaps resulting from missing data. The anti-log was then taken of the block-averaged and smoothed CHL fields prior to computation of the anomaly fields. The raw anomalies are analyzed here, instead of the log-transformed anomalies, because the magnitude of the raw anomalies can be converted into units of mg m^{-3} using Eq. (3). This choice is supported by a detailed analysis (Appendix B of Gaube et al., 2013) which showed diagnosis of mesoscale CHL variations in South Indian Ocean eddies was insensitive to the use of log-transformed or raw anomalies.

Chlorophyll anomaly fields (CHL') are defined as:

$$\mathrm{CHL}' = \mathrm{CHL} - \langle \mathrm{CHL} \rangle, \tag{2}$$

where the ⟨CHL⟩ denotes the 6°×6° smoothed fields that are removed from the total fields to create anomalies denoted by primes.

Fields of CHL' are suitable for computing direct correlations with SLA (Section 5.1) but compositing multiple observations into CMS-centric coordinates (Section 5.2) poses an additional challenge. Specifically, the magnitude of the eddy-driven CHL anomalies varies both geographically and seasonally. To help mitigate these effects on CMS-centric composites, we normalized the anomalies at longitude x and latitude y by the long-term averaged background fields at the same location,

$$\text{CHL}''=\frac{CHL'(\text{x, y})}{\overline{\text{CHL}(\text{x, y})}}, \tag{3}$$

where $\overline{\text{CHL}(\text{x, y})}$ is the time-averaged background CHL field. The normalized CHL anomalies are denoted by the double-primes.

The evolution of CHL'' and CHL' in CMS (Section 5.2) are used to help distinguish between different mechanisms that influence the chlorophyll response. Time series of CHL'' and CHL' are constructed from composite averages within a radial distance of $0.5L_s$ of the CMS SLA extremum (see Section 3.4 for the definition of L_s). To investigate changes in CHL' following CMS formation, time series of CHL' relative to CMS detection (ΔCHL') are constructed by subtracting the CHL' at the time of CMS detection from each subsequent weekly realization of CMS-centric CHL':

$$\triangle CHL'(\text{k}) = CHL'(\text{k}) - CHL'(\text{k} = 1), \tag{4}$$

where k is the age of the CMS, in 5-day time steps. Time series of ΔCHL' from satellite observations were limited to individual CMS realizations that contained at least one third of the total possible pixels within a radial distance of L_s from the CMS SLA extremum.

In some regions, satellite observations of ocean color may include radiance from subsurface CHL maxima. In such situations, the comparison of satellite estimates of CHL to surface CHL from a coupled physical/biological simulation might not be appropriate. Subsurface chlorophyll maxima have been observed at depths between 30 and 50 m in warm core rings (Hitchcock et al., 1985). In the slope region where these warm core rings occur, the first optical depth (estimated from the inverse of the diffuse attenuation coefficient at 490 nm) ranges from 10 to 25 m in summer and 5 – 15 m in winter (not shown). Surveys of cold core rings in the Sargasso Sea reveal the presence of a deep chlorophyll maximum between ~ 50 – 70 m (Wiebe et al., 1976). In this region, the first optical depth ranges from 25 to 40 m (not shown). Additionally, cold core rings are observed to have enhanced CHL and thus the optical depth is shallower within the rings when compared to the surrounding oligotrophic waters. Thus, it does not appear likely that the satellite estimates of CHL used herein include significant contributions from subsurface chlorophyll maxima, as such features typically reside too deep to affect the satellite retrievals.

3.2. *Observations from the World Ocean Atlas*

Optimally interpolated observations of nitrate concentration (Garcia et al., 2014) and temperature (Locarnini et al., 2013) archived in version 2 of the 2013 edition of the World Ocean Atlas were downloaded from the National Center for Environmental Information.

3.3. *The model*

The coupled physical/biological model used in this study is described in detail in Anderson et al. (2011). Briefly, the physical model is based on the Los Alamos Parallel Ocean Program (POP) and configured for the North Atlantic (20°S–70°N) using an eddy-resolving grid with horizontal spacing of 11.1 cos(ϕ) km, where ϕ is latitude. This results in a zonal grid spacing of 9.6 km at 30°, 8.5 km at 40° and 7.1 km at 50°. Horizontal mixing processes are parameterized with a biharmonic operator and vertical viscosities and diffusivities are computed based on the Richardson number formulation described by Pacanowski and Philander (1981). Details of the subgrid-scale parameterizations are described in McGillicuddy et al. (2003).

The biological module is the 24-box biogeochemical element cycling (BEC) model that includes three phytoplankton groups: diatoms, small phytoplankton and diazotrophs and a single zooplankton community that grazes upon the three phytoplankton classes (Moore et al., 2004, 2006; Moore and Doney, 2007). A complete list of the equations used in the BEC model can be found in Moore et al. (2002). The source code of the BEC ecosystem module used in this study is included in the online electronic supplement. Although this representation of the grazing community is highly idealized, it is suitable for the present study in which we focus on bottom-up rather than top-down controls on the phytoplankton population. The limiting nutrients are nitrate (NO_3), ammonium (NH_4), phosphate (PO_4), iron (Fe), and silicate (SiO_3). The model includes sources and sinks of nutrients including nitrogen fixation by diazotrophs, denitrification, and the deposition of particulate matter into the sediments. The parameters of the BEC model were tuned to observations in the North Atlantic from the Bermuda Atlantic Time Series and the North Atlantic Bloom Experiment (Anderson et al., 2011).

Temperature, salinity and macronutrients were initialized from the World Ocean Atlas 2001 (Boyer et al., 2002; Conkright et al., 2002; Stephens et al., 2002; Locarnini et al., 2006). Dissolved inorganic carbon and alkalinity were initialized with concentrations from the GLODAP climatology (Key et al., 2004). The other biological state variables were initialized from year 800 of a coarse-resolution global model. The eddy-resolving simulation is forced at the surface using annually repeating "normal year" atmospheric forcing (Large and Yeager, 2004) and was run for 14.5 years to achieve a quasi-equilibrium state. The biological parameters were then tuned to improve agreement with observations, and NO_3, PO_4, SiO_3 and O_2 were re-initialized with climatological July values (Anderson et al., 2011). The coupled model was run for an additional 7 years, of which the final 5.5 years are analyzed here.

The model is run in two different configurations, differing only in the formulation of the surface stress $\boldsymbol{\tau}$. The first simulation is forced by a large-scale, annually repeating wind $\boldsymbol{u}_{air}$:

$$\boldsymbol{\tau} = C_D \rho_a \boldsymbol{u}_{air} |\boldsymbol{u}_{air}|, \tag{5}$$

where C_D is a speed-specific drag coefficient and ρ_a is the density of air. The second simulation includes the influence of ocean surface currents $\boldsymbol{u}_{sea}$ on the surface stress forcing:

$$\boldsymbol{\tau} = C_D \rho_a (\boldsymbol{u}_{air} - \boldsymbol{u}_{sea}) |\, \boldsymbol{u}_{air} - \boldsymbol{u}_{sea} \,|. \tag{6}$$

Because the surface stress curl has a polarity opposite to that of the vorticity of eddy surface currents, the inclusion of $\boldsymbol{u}_{sea}$ in the formulation of $\boldsymbol{\tau}$ generates Ekman upwelling in the cores of anticyclonic eddies and downwelling in the cores of cyclonic eddies (see Section 2). By comparing the solutions of these two simulations, we are able to assess the influence of eddy-induced Ekman pumping on the mesoscale variability of CHL in the study region. It is important to note that the two different formulations of the surface stress also affect the mean circulation (*e.g.*, Hutchinson et al., 2010). These differences are not investigated here.

3.4. *The identification and tracking of coherent mesoscale structures*

CMS are identified following the method outlined in detail in Appendix B2 of Chelton et al. (2011b). A closed contour of SLA is identified as a CMS if it meets the following criteria: (1) At least one local maximum (minimum) of SLA for anticyclonic (cyclonic) CMS exists within the closed contour. (2) The SLA at the local extrema is greater (less) than zero for anticyclones (cyclones). (3) The amplitude of the CMS, defined as the difference between the SLA extremum in the CMS interior and the SLA value along the outermost closed contour of SLA, is at least 1 cm. (4) The distance between any pair of points within the connected region must be less than 500 km. (5) The speed-based eddy radius, L_s(see below), of a CMS must be in the range $40km \leq L_s \leq 250km$.

CMS are tracked in time using a method based on the one described in Appendix B4 of Chelton et al. (2011b). For every CMS SLA extremum identified at time step t, the CMS identified at the next time step $t + 1$ are searched to find the closest CMS lying within a restricted search region consisting of an ellipse with a zonally oriented east-west semi-major axis of 100 km and a north-south semi-minor axis of

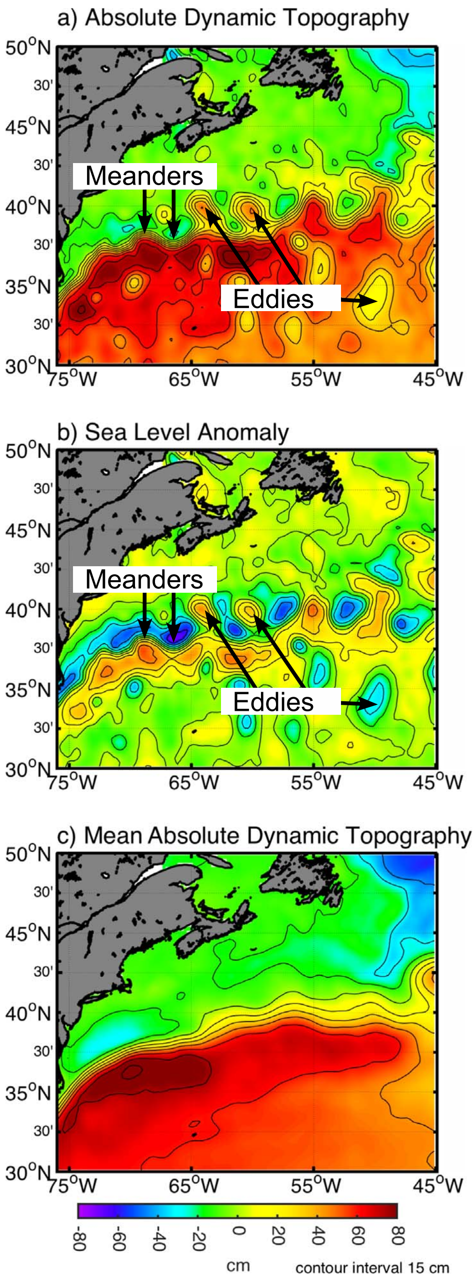

Fig. 1. Maps of (a) absolute dynamic topography (ADT) and (b) sea level anomaly (SLA) from merged satellite observations for the week of 1 January 2012. (c) Map of the 22-year mean absolute dynamic topography (MDT). SLA in panel b is high-pass filtered using a loess filter with a half-power cutoff of 20° in longitude and 10° in latitude (see Section 3.1 for details). The location of a series of eddies and meanders are indicated by the black arrows in panels a and b. The sea level observations shown here were produced by AVISO/CLS; see Section 3.1 for details on the methods.

75 km. If no CMS are found at the time step $t+1$, CMS at time step $t+m$, where $m=2{,}3$, are searched for within an ellipse with the semi-major east-west axis of m*100 km and a semi-minor north-south axis of 75 km.

Tracked CMS are characterized by several variables. As described above, the CMS amplitude at each 5-day time step along its trajectory is defined to be the difference between the SLA extremum in the CMS interior and the SLA value along the CMS perimeter, delineated as the outermost closed contour of SLA that defines it compact structure. The CMS interior is defined to be the region inside this SLA contour. The horizontal speed-based radius scale of the CMS, L_s, is defined to be the radius of a circle with area equal to that enclosed by the SLA contour around which the average geostrophic speed is maximum within the CMS interior.

In Section 5 we investigate the different influences of eddies and meanders on CHL. The signature of eddies and meanders in maps of absolute dynamic topography (ADT, Fig. 1a), defined as the sum of SLA (Fig. 1b) and the mean dynamic topography (MDT, Fig. 1c), are distinct: eddies are characterized as closed contours of ADT surrounding an SLA extremum, whereas meanders consist of undulating ADT contours (Fig. 1a). Both types of features are expressed in SLA (Fig. 1b), and they can be differentiated based on their direction of propagation: meanders generally propagate eastward while isolated eddies generally propagate westward (Fuglister, 1972; Richardson, 1980). In this study, we define a CMS as being either an eddy or meander using the following criteria: If the net zonal displacement of a CMS is westward, it is defined as an eddy, whereas if it is eastward, it is defined as a meander. Because some GS meanders become eddies, we define transformation of a meander into an eddy after 4 consecutive weeks of westward propagation. Likewise, an isolated westward propagating eddy can be reabsorbed by the GS, becoming a meander. We allow eddies to become meanders after 4 consecutive weeks of eastward propagation. The age (k) of meanders that pinch-off as eddies, or eddies that are reabsorbed as meanders, are defined relative to the first week of westward or eastward propagation, respectively.

It is important to note that the zonal propagation characteristic of eddies and meanders in the Gulf Stream region are complex and the simple criteria used to differentiate these two types of features used here may lead to the misclassification of individual CMS. Richardson (1980) observed eddies being advected eastward when they came into contact with the Gulf Stream. These eddies were either absorbed by the Gulf Stream or eventually split off and continued their westward propagation. On average, however, eddies interacting with the Gulf Stream were observed to propagate eastward for less than 3 weeks (Richardson, 1980), and therefore would not be misclassified as meanders in this study.

The GS region is defined here by an envelope with northern and southern boundaries 2° north and 7° south of the north wall, which enclose the area of large CMS amplitudes associated with the GS (Fig. 2c, f and i). The GS north wall was defined by the mean location of the 15° isotherm at 200 m, as suggested by Fuglister (1963), and is indicated by a solid black curve in all panels. The observed GS north wall was computed from climatological temperature profiles collected in version 2 of the 2013 edition of the World Ocean Atlas (Locarnini et al., 2013). The eastern and western boundaries of the GS region are defined by the 70°W and 43°W meridians, respectively. Eddies of the GS are included in this study if they originate within this envelope and are only considered when their SLA extremum remains within this envelope. It is important to note that both open-ocean eddies and rings generated by the pinching-off of GS meanders are observed in this region. Since the primary focus of this study is to diagnose the mechanisms generating the observed CHL response to CMS in the GS region, both eddies and rings are analyzed together, distinguished only by their polarities (cyclonic and anticyclonic).

Meanders of the GS are similarly defined, but with the southern boundary of the envelope limited to 3° south of the GS north wall (see dashed lines in panels c, f and i of Fig. 2). This truncated subregion was chosen after animations of CMS revealed that some eddies in the southern portion of the GS region propagated eastward as a result of eddy/eddy interaction.

To evaluate the CHL response to mesoscale eddies and meanders, satellite and model-derived estimates of CHL'' and CHL' are collocated to the interior of each CMS for the 5-year study period. The collocated values are interpolated onto a high-resolution grid by scaling the distances from each eddy SLA extremum to all grid points in the eddy interior by the eddy radius L_s. This normalization allows composites to be constructed from thousands of weekly CMS observations on a common grid defined by the horizontal size of each individual CMS.

The location of CHL anomalies associated with meander-induced vertical motion, relative to the SLA extremum of GS meanders,

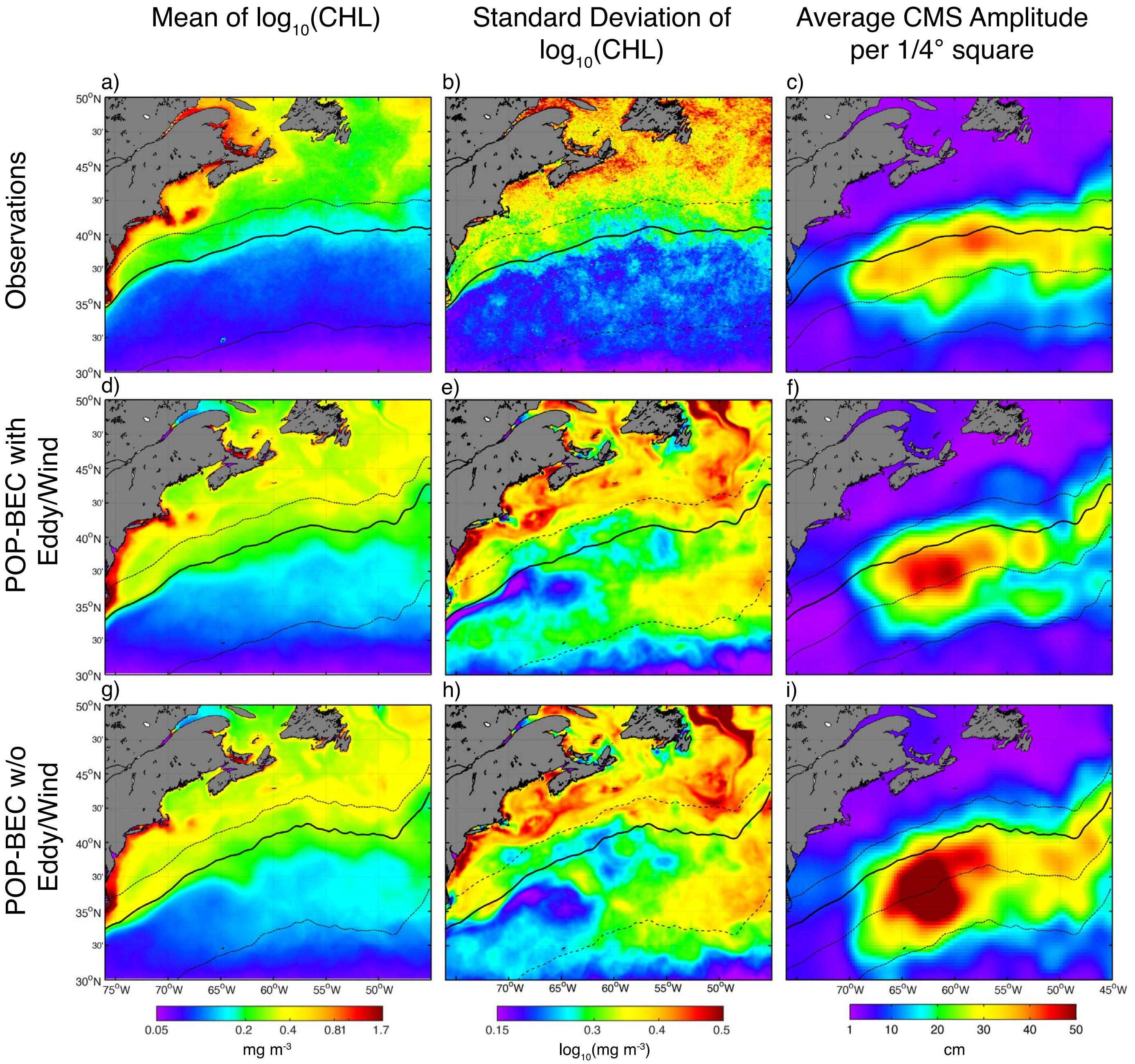

Fig. 2. Maps of the mean (left column) and standard deviation (middle column) of the $\log_{10}$-transformed CHL fields. The average coherent mesoscale structure (CMS) amplitude per ¼° square is shown in the right column. Satellite observations are shown in the top row, data from the model with eddy-induced Ekman pumping in the middle row, and data from the model without eddy wind interaction in the bottom row. The solid lines and northern and southern most dashed curves are described in the caption of Fig. 3. In panels c, f and i, the dashed curve located 3° south of the GS north wall delineates the region in which meanders are identified (see Section 3.4).

depends in part on the orientation of the GS. To account for spatial variation in GS orientation, meander-centric composite averages were constructed from CHL'' rotated to align the mean GS north wall (see Fig. 2), averaged zonally within 4° of the meander SLA extremum, to a polar angle of 0°. It turns out that the rotated and non-rotated CHL'' composites are qualitatively similar, and thus the results are not sensitive to this aspect of the procedure.

4. Characteristics of the Gulf Stream region: from the large-scale to mesoscale

The time-averaged, basin-scale surface CHL fields generated in both simulations have a geographic structure that is similar to observations in the GS region: a general north-northwestward gradient with the largest magnitude of the open-ocean spatial CHL gradient occurring in the region of the GS north wall (Fig. 2a, d and g). The magnitude of the time-averaged CHL, however, is larger in the BEC simulations, with the largest mean CHL occurring in the simulation without eddy-induced Ekman pumping (Fig. 2g, note that the $\log_{10}$ transform of CHL is shown). The standard deviation of the CHL ($\sigma(CHL)$) in the simulations differs substantially from observations (Fig. 2b, e and h). Most noticeably, both simulations have a local maximum of $\sigma(CHL)$ southeast of the GS, centered at approximately 35°N, 45°W, which is not present in the ocean color observations. Additionally, observed $\sigma(CHL)$ is substantially noisier than the simulated fields. To assess the degree of which this is a result of missing data (clouds), the simulated CHL fields were masked to remove data not present in the observations. The resulting cloud-masked simulated

$\sigma(CHL)$ were only slightly nosier than the full $\sigma(CHL)$ fields (not shown) and still contained large coherent structures in $\sigma(CHL)$ that were not visible in the observations. Therefore, we conclude that the large differences between the observed and simulated CHL fields likely result from model errors. Despite these differences in the variability of the CHL field between the simulation and observations, the cross

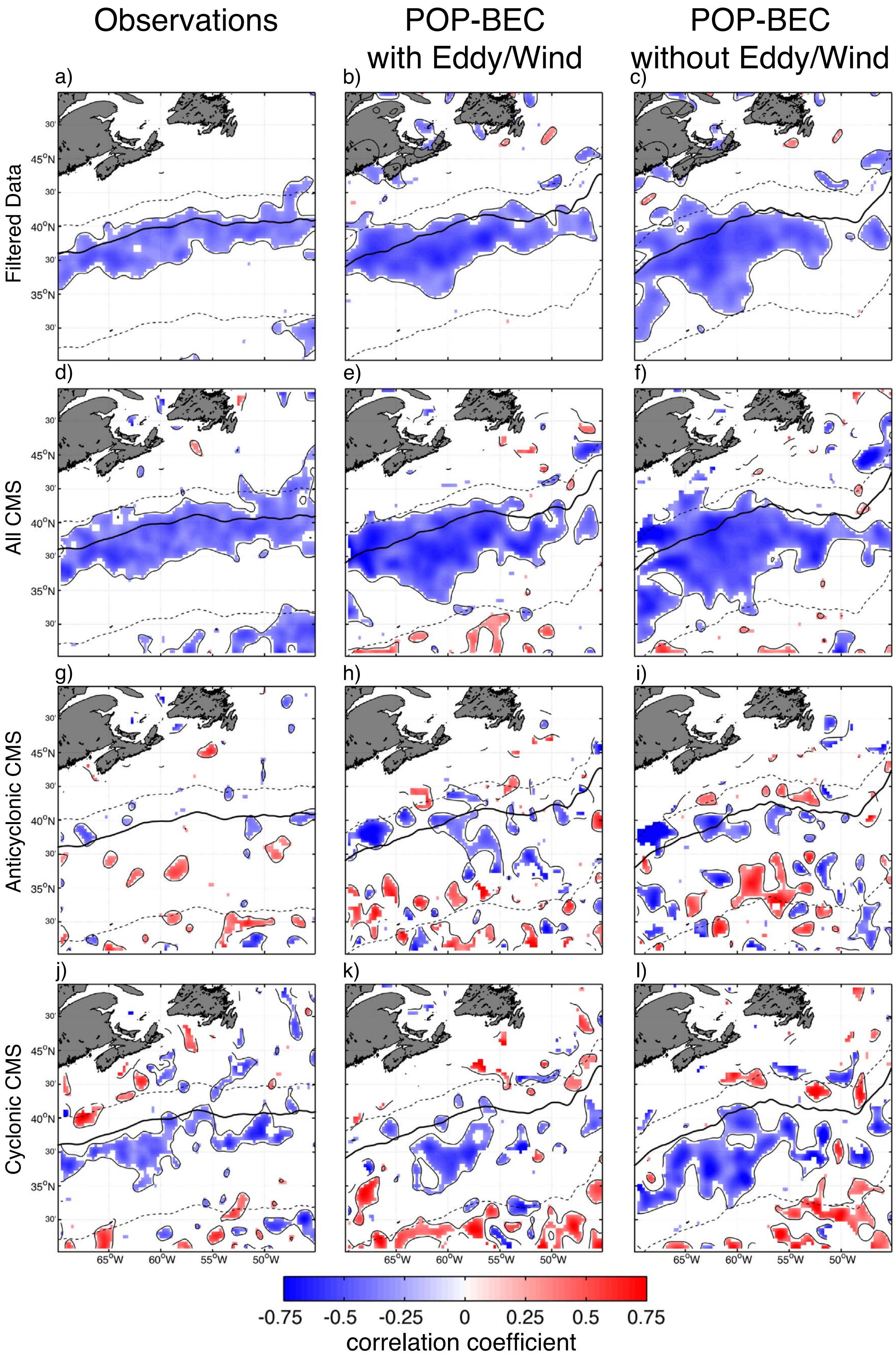

Table 2
Half-saturation constants (k) of macro nutrients in the simulation with eddy-induced Ekman pumping and their composite-averaged values in the cores of anticyclonic and cyclonic eddies. All concentrations reported in units of mmol m^{-3}.

	NO_3	NH_4	PO_4
k Diatoms	2.5	0.08	0.02
k Small Phytoplankton	0.5	0.005	0.005
Anticyclonic Eddies	0.9	0.025	0.06
Cyclonic Eddies	1.2	0.055	0.09

correlations between SLA and CHL' are similar (Fig. 3).

To assess if phytoplankton in the GS region are nutrient limited, and during what seasons, we compare observations from the World Ocean Atlas and the simulated surface concentration of nitrate (NO_3) to the half-saturation constants for uptake used in the model (Table 2). During the summer, observed surface [NO_3] ranges from 0 to 0.75 mmol m^{-3} (Fig. 4b) which is below the half-saturation constant for nitrate uptake by diatoms throughout the domain and below that for small phytoplankton in most of the region. This suggests that over most of the study domain, phytoplankton growth is limited by NO_3 in summer. The simulated summertime surface NO_3 concentrations are generally lower than observed, and thus nutrient limitation may be overestimated in the model. During the winter, when light limitation can eclipse nutrient limitation in much of the GS region, the surface NO_3 concentration reaches 4–7 mmol m^{-3} over the shelf and north of the Gulf Stream, yet remains below the half-saturation constant for uptake by both diatoms and small phytoplankton to the south of the Gulf Stream (Fig. 4a). Both of the model solutions generate this northward gradient in NO_3 during the winter, however the concentrations over the shelf are two to three times larger than observed (Fig. 4c,e). Nevertheless, the region south of the Gulf Stream, which encompasses the largest area of focus for this study, observed and simulated NO_3 concentrations generally fall within a range that limits phytoplankton growth throughout the year (Fig. 4).

The physical characteristics of eddies and meanders in the two simulations are compared to observations by analysis of the SLA amplitude, radius scale L_s, and CMS lifetime (Fig. 5). The average amplitudes of CMS in the GS region are approximately 20 to 40 times the 1 cm detection limit described in Section 3.4, suggesting that these features are robust and not merely the result of noise in the SLA fields. The mean amplitude of meanders and eddies in the models and observations are similar, although some significant differences in eddy amplitude exist. First, the mean amplitudes of eddies in the simulation including eddy-induced Ekman pumping are smaller than the simulation without eddy-induced Ekman pumping (Fig. 5d and g).

This is expected as eddy-induced Ekman pumping tends to attenuate eddies (Dewar and Flierl, 1987; Eden and Dietze, 2009; Gaube et al., 2015). Second, cyclones trackedin satellite observations are systematically larger in amplitude than anticyclones (Fig. 5a). This asymmetry is reproduced in the two simulations, but to a much lesser degree (Fig. 5d and g). The percentage of eddies with amplitude larger than ~ 22 cm is greater in the simulation without eddy-induced Ekman pumping when compared to observations and the simulation that includes the eddy surface current effect on the surface stress (Fig. 5j). The geographic structure of CMS amplitude in the two different simulations is similar to observations, with the largest amplitudes occurring in the GS region (Fig. 2c, f and i). However, the simulated CMS display a local maximum in amplitude that is displaced to the southwest of the maximum in the observations. This aspect was also noted by Bryan et al. (2007) [see their Figure 12], which may be a result of bias in the interaction of the Gulf Stream with topography in the vicinity of the New England Seamount Chain (F.O. Bryan, personal communication).

The simulated CMS are generally larger in radius than the observations (Fig. 5b, e and h), with the exception of cyclonic meanders in the simulation including eddy-induced Ekman pumping, which are similar in radius to the observations. Anticyclonic eddies are observed to be, on average, larger in radius than cyclones, with eddies larger than 100 km being predominantly anticyclonic (Fig. 5b and k). This asymmetry in radius scale is reproduced in both simulations with the largest degree of asymmetry being generated in the simulation that does not including eddy-induced Ekman pumping (Fig. 5h and k).

Cyclonic GS eddies are observed to live longer than anticyclonic eddies, an asymmetry that is reproduced in both simulations (Fig. 5c, f and i). The average lifetimes of observed eddies are longer than the lifetimes of eddies in the simulations. The distribution of lifetime for both observed and simulated eddies in our study indicate a larger proportion of long-lived eddies, when comparted to the analysis of eddies in a 50-year simulation conducted by Kang and Curchitser (2013). The lifetimes of meanders in our analysis, however, are shorter and comparable to the "eddies" of Kang and Curchitser (2013). This suggests that many of the CMS described as eddies in the study by Kang and Curchitser (2013) might actually be meanders, which is supported by the presence of a large number of eastward-propagating trajectories in their Fig. 8. It is interesting to note that the lifetimes of eddies in the simulation including eddy-induced Ekman pumping are significantly longer than their counterparts in the simulation without eddy-induced Ekman pumping interaction (Fig. 5f and i). Similarly, the lifetimes of meanders in the simulation including eddy-induced Ekman pumping are also longer than in the other simulation. This is somewhat puzzling, at least for the case of eddies, because eddy-induced Ekman pumping tends to systematically attenuate eddies. This suggests that in the GS region, eddy lifetimes may be controlled by mechanisms other than eddy-induced Ekman pumping. The average eddy amplitude at the end its lifetime is rather large (> 20 cm, Fig. 6), 20x the level of detection. Thus, the fate of the average eddy is not to decay to zero amplitude, but rather to merge with another eddy or reabsorb into the GS. Therefore, eddy-induced Ekman pumping does not appear to exert direct control on eddy lifetime.

5. The influence of coherent mesoscale structures on chlorophyll

The influence of CMS on CHL in the GS region is investigated in the following sections by employing 3 different analysis techniques: investigation of the cross correlation of SLA and CHL' (Section 5.1), comparisons of the spatial structure (Section 5.2), and temporal evolution (Section 5.3) of composite averages constructed in CMS-centric coordinates.

5.1. Cross correlation of SLA and CHL'

The response of the phytoplankton community to physical/biological forcing occurring in CMS can result in significant cross correlation

Fig. 3. Maps of the cross correlation of SLA and CHL' at 0 time lag within the study domain (30°N–50°N, 76°W–45°W). White areas correspond to correlations smaller than the estimated 95% significance level, calculated following the standard formula (Von Storch and Zwiers, 1999). We estimate the effective degrees of freedom as the number of month of data (N*=67). Regions of significantly positive cross correlation ($r \geq 0.24$) are enclosed by a solid contour and regions of significantly negative cross correlation ($r \leq 0.24$) are enclosed by a dashed contour. Correlation coefficients computed from satellite observations of SLA are shown in the left column, the model with eddy-induced Ekman pumping in the middle column and model without eddy wind interaction in the right column. The correlation coefficients of the high-pass filtered data are shown in row 1; correlation coefficients computed from data limited to the interiors of CMS are shown in row 2; correlation inside anticyclonic CMS in row 3; and correlation inside cyclonic CMS in row 4. The northern and southern dashed curves indicate the GS north wall plus 2° and minus 7°, respectively (see Section 3.4). Note that all high-resolution model output was interpolated to the1/4° latitude by 1/4° longitude grid of the satellite observations prior to computation of correlation coefficients.

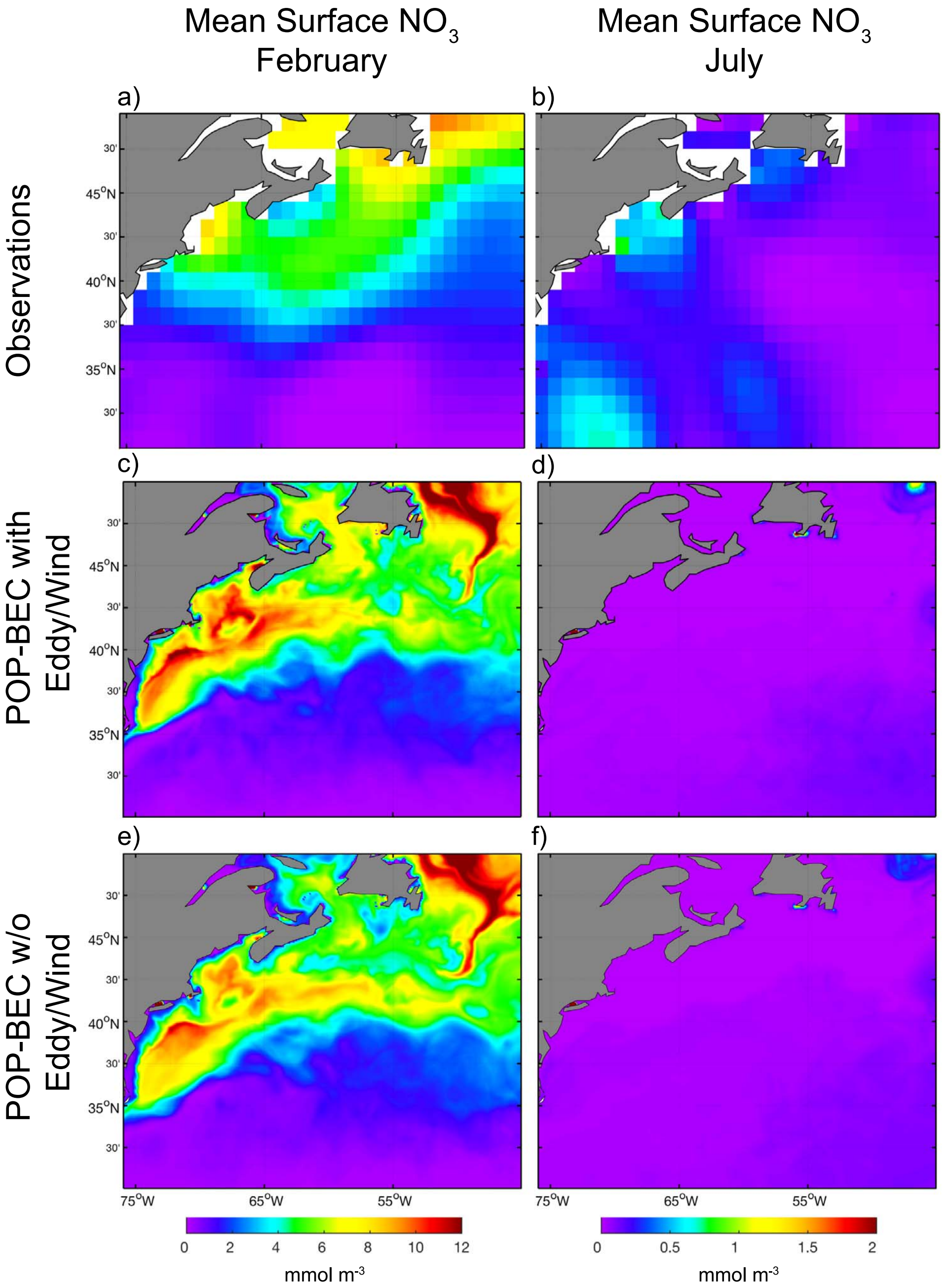

Fig. 4. Maps of the mean surface NO_3 concentration from the World Ocean Atlas in the top row, the model with eddy-induced Ekman pumping in the middle row, and the model without eddy wind interaction in the bottom row. The left column of panels show average values in February and the right column averages in July. Note different colorbar scaling between the two columns of panels.

of SLA and CHL' (Chelton et al., 2011a; Gaube et al., 2014). The correlation of time series of SLA and CHL' at a single location provides information on the relationship between these two quantities as eddies propagate through. For example, if the passing of a cyclonic eddy (negative SLA) is associated with elevated CHL (positive CHL'), the cross correlation will be negative. In general, the GS region is characterized by negative cross correlation of SLA and CHL' (Fig. 3a). Negative correlation implies that elevated CHL is associated with cyclonic CMS (negative SLA) and suppressed CHL with anticyclonic CMS (positive SLA). The geographic structure of correlation in the satellite observations consists of a band of significantly negative correlation centered to the south of the GS north wall (Fig. 3a). Both simulations reproduced the general geographic structure and magnitude of the observed negative correlation, but in the simulations, the area of significant negative correlation is larger in the west and smaller in the east (Fig. 3b and c). When limiting the correlation to the interior of CMS, the general geographic structure of observed correlation within the GS region is not significantly altered, however its magnitude is slightly increased and the spatial extent of the region of negative correlation to the southeast of the GS is increased (Fig. 3d). The simulations, however, do not generate this southeastern region of negative correlation and produce regions of significant positive correlation to the south of the GS region that are not observed in the satellite observations (Fig. 3e and f).

To investigate if the observed correlation is a result of processes occurring in cyclonic or anticyclonic CMS, we compute the correlation from observations limited to the interiors of anticyclonic or cyclonic CMS. Within anticyclonic CMS, a few spots of negative correlation are observed north of the GS north wall, where warm-core GS rings are observed, and positive correlation to the south of the GS north wall

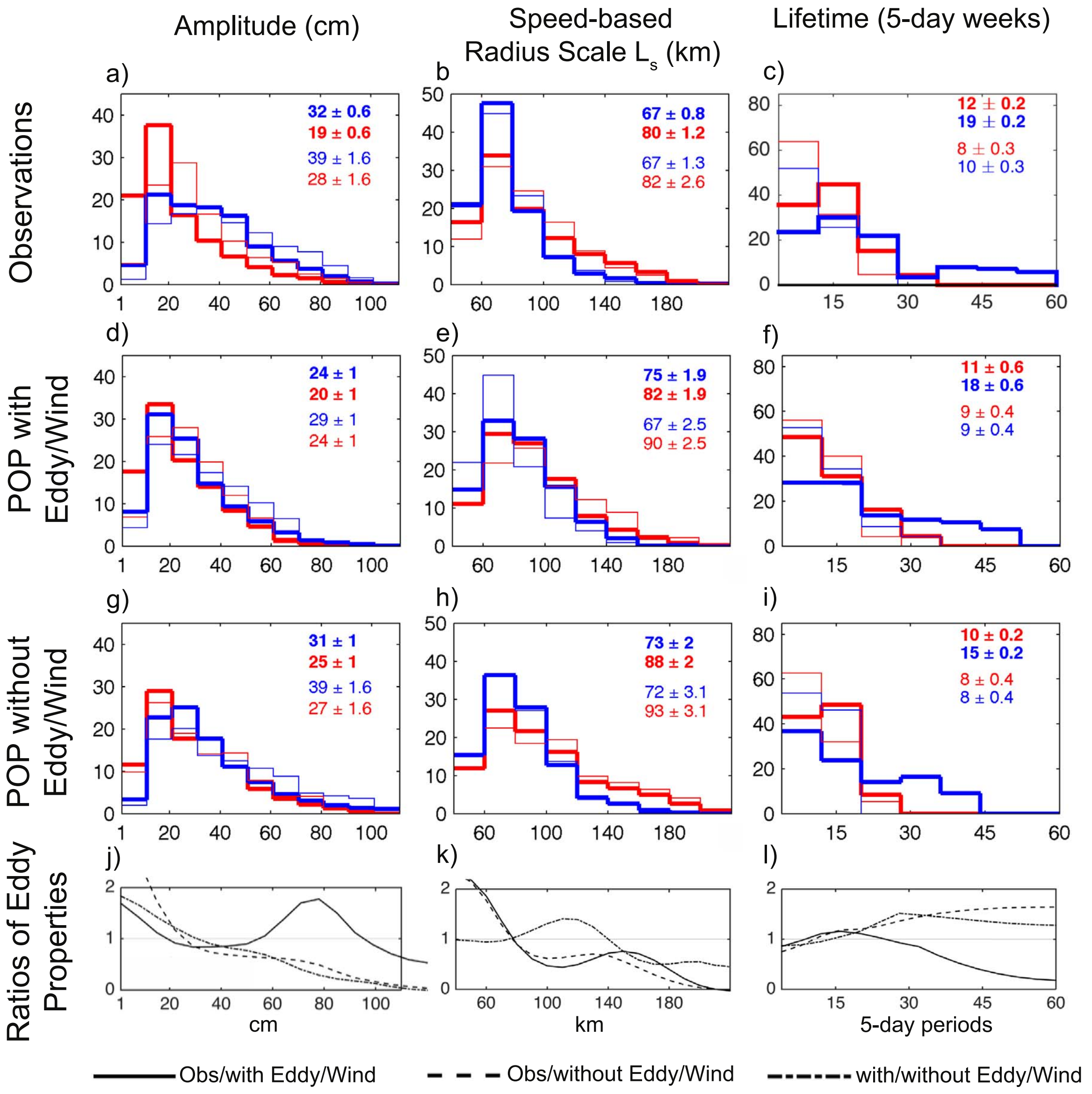

Fig. 5. Histograms of eddy and meander amplitude (left column), speed-based radius scale L_s (middle column) and lifetime (right column), reported as the number of 5-day periods, the temporal resolution on which the model solutions are archived. Histograms of anticyclonic and cyclonic eddies are shown as thick red and blue lines, respectively. Histograms of anticyclonic and cyclonic meanders are shown as thin red and blue lines, respectively. Eddies and meanders tracked in satellite observations of SLA are shown in the top row, the model with eddy-induced Ekman pumping in the middle row and model without eddy wind interaction in the bottom row. Mean values and 95% confidence interval for eddies (bold text) and meander are shown in the upper right corner of each panel. The bottom row of each panel shows the ratio of the eddy histograms in the upper three rows. The ratio of eddy properties in the observations to those in the solution with eddy-induced Ekman pumping is shown as a solid line; the corresponding ratio for the observations to the solution without eddy-induced Ekman pumping is a dashed line, and the ratio for the two solutions is a dashed-dotted line.

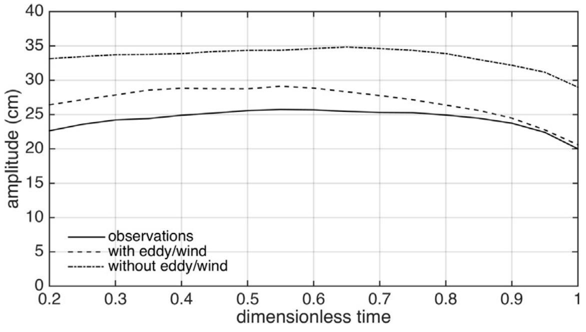

Fig. 6. Amplitude time series of observed eddies (solid curve), eddies in the simulation with eddy-induced Ekman pumping (dashed curve), and the simulation without eddy-induced Ekman pumping (dashed and dotted curve). The *x* axis has been normalized by the lifetime of the eddies.

(Fig. 3g). The regions of negative correlation are larger in magnitude and spatial extent in both simulations (Fig. 3h and i) and expand further to the south in the simulations including eddy-induced Ekman pumping (Fig. 3h). It is interesting to note that both simulations generate regions of significant positive correlation south of the GS (Fig. 3h and i), which can be generated by eddy-induced Ekman pumping (Gaube et al., 2014). Positive correlation south of the GS, however, is also generated in the simulation without eddy-induced Ekman pumping, suggesting that other mechanisms likely result in the observed positive correlation in these regions.

Observed cyclonic CMS generate a large region of negative correlation south of the GS north wall (Fig. 3j), where cold-core cyclonic GS eddies form and propagate westward. Both simulations reproduce the general structure of the region of negative correlation, however, it is somewhat compressed zonally in the simulation with eddy-induced Ekman pumping (Fig. 3k) and expanded meridionally in the simulation

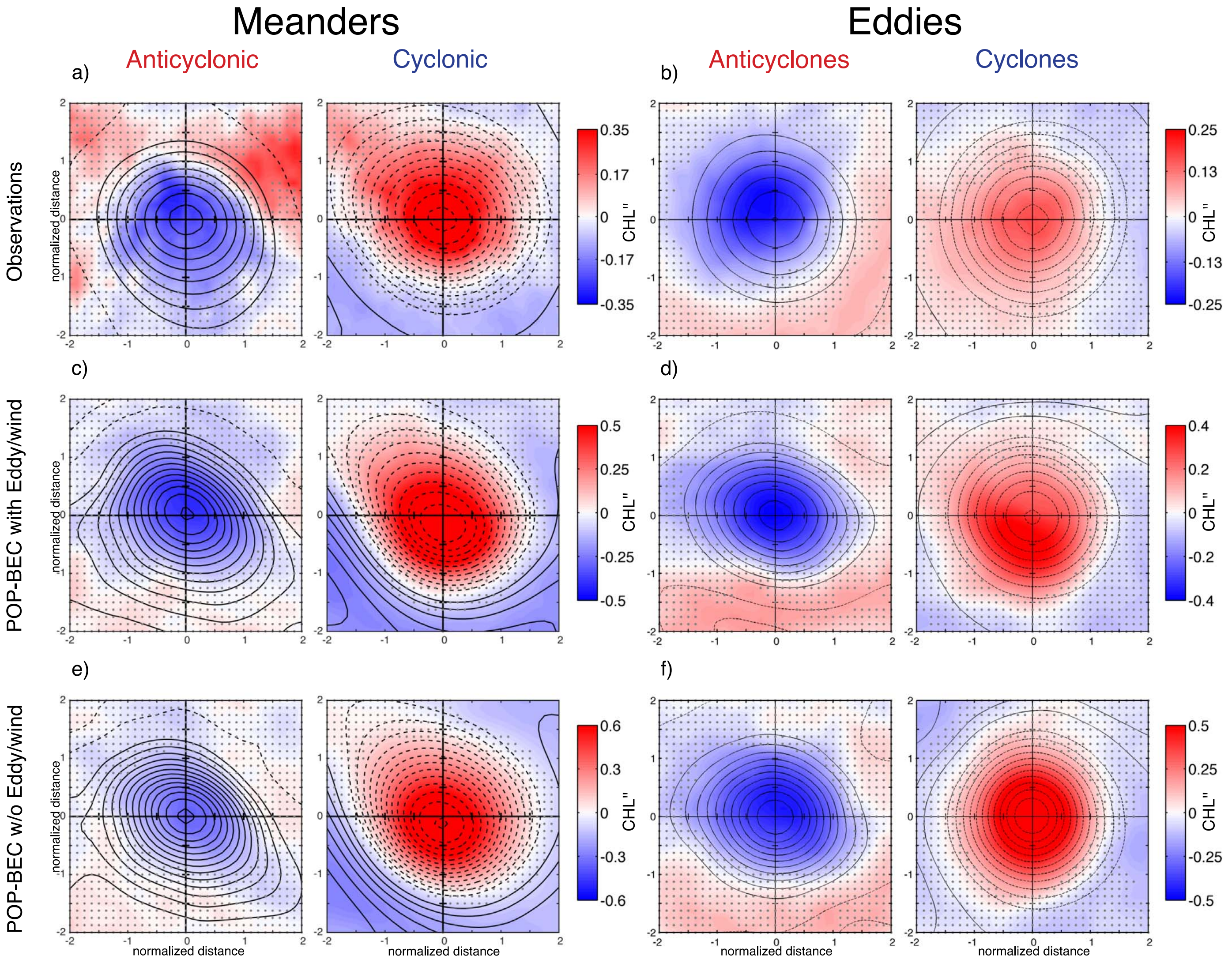

Fig. 7. Composite averages of normalized CHL anomalies (CHL") overlaid with contours of SLA. Rotated composite averages (see Section 3.4) of anticyclonic and cyclonic meanders are shown in columns 1 and 2, respectively, and nonrotated composite averages of anticyclonic and cyclonic eddies are shown in columns 3 and 4, respectively. Composite averages from satellite observations are shown in the top row, from the model with eddy-induced Ekman pumping in the middle row and from the model without eddy-induced Ekman pumping in the bottom row. The x and y axes of the individual composites have been normalized by the speed-based radius scale L_s. Grey stippling indicates regions of the composite average that do not exceed the 95% confidence interval of the mean.

without eddy-induced Ekman pumping (Fig. 3l). There are multiple regions of positive correlation located around the line depicting 7° south of the GS north wall in both simulations (Fig. 3k and l). Regions of positive correlation are also visible in the satellite data (Fig. 3j), however these regions are smaller in magnitude and spatial extent.

5.2. Composite averages of CHL"

The spatial structure of the rotated composite averaged CHL" in anticyclonic eastward propagating meanders consists of a monopole of negative CHL" collocated with the composite averaged SLA extrema (Fig. 7a, left panel). The monopole of negative CHL" in anticyclones is consistent with the northward transport and subsequent trapping of low CHL from the Sargasso Sea. Composite averaged CHL" in cyclonic meanders consists of a monopole of positive CHL" collocated with the composite average SLA minima and a secondary region of negative CHL" located to the south (Fig. 7a, right panel). This spatial structure is consistent with the southward transport and subsequent trapping of high CHL slope water. It is interesting to note that the monopole of negative (positive) CHL" observed in anticyclonic (cyclonic) GS meanders that dominates the composite averages in Fig. 7a differs from the patterns in CHL" expected from submesoscale patches of upwelling and downwelling in meanders. One explanation could be that the orientation of such CHL anomalies in meander-centric coordinates is so variable that these signals are averaged out in the compositing procedure. Alternatively, the CHL response to submesoscale vertical velocities could be masked by the large gradient of CHL across the GS that is reflected in the monopoles of CHL" observed here. Furthermore, the biological response may often be limited to deeper portions of the euphotic zone, and therefore not observed in near-surface CHL. Lastly, the resolution of the observations and the model may not be sufficient to observe the CHL response to submesoscale upwelling —although such patterns have been detected in some synoptic images (Olson et al., 1994).

The geographic structure of composite averaged CHL" in westward propagating GS eddies consists primarily of monopoles of negative and positive CHL" in anticyclones and cyclones, respectively (Fig. 7b). This is consistent with the trapping of water with low (high) CHL into anticyclones (cyclones) undergoing formation. These monopolar CHL" are also in agreement with the expected CHL response to downwelling and upwelling occurring during the intensification of anticyclones and cyclones, respectively.

Both simulations reproduced the general structure of observed

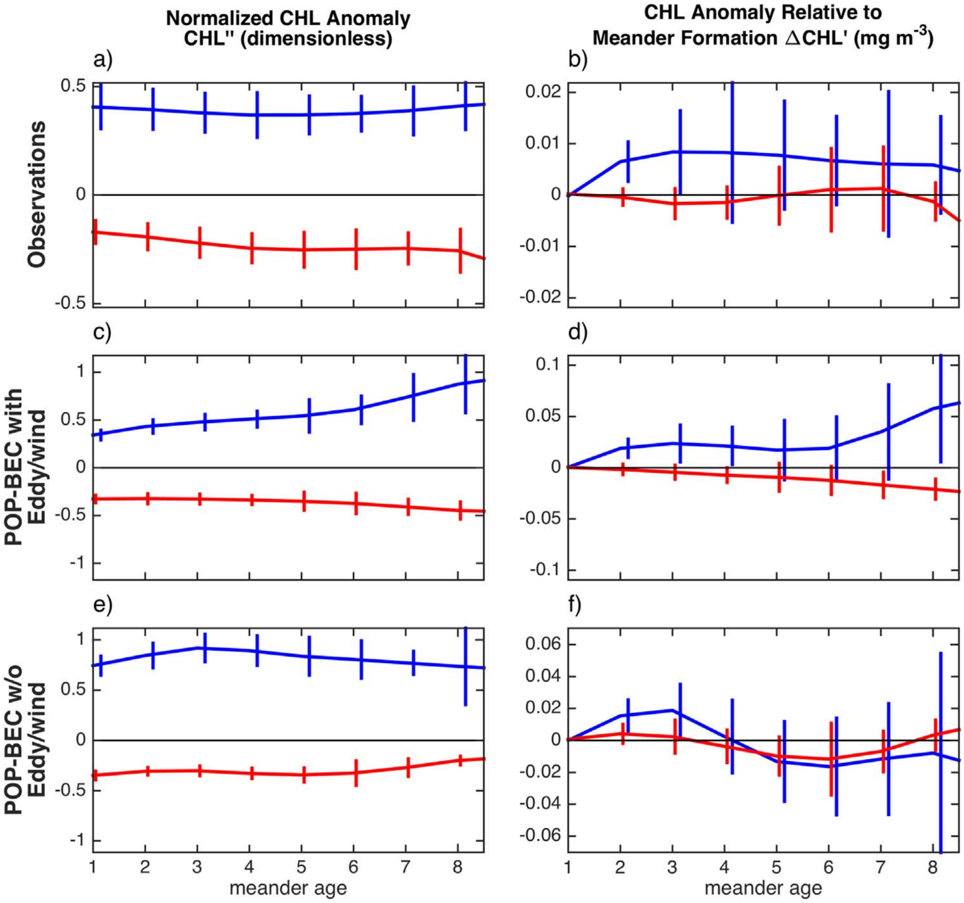

Fig. 8. Composite average time series within a radial distance of 0.5L_s of the SLA extremum of eastward propagating anticyclonic meanders (red) and cyclonic meanders (blue) bin averaged as a function of meander age (in number of 5-day periods). Time series of satellite observations are shown in the top row, the model with eddy-induced Ekman pumping in the middle row, and model without eddy-induced Ekman pumping in the bottom row. Times series in the left and right columns are of normalized CHL anomalies (CHL'') and CHL' relative to the CHL' at the time of meander formation (ΔCHL'), respectively. The vertical bars represent the standard error of the mean computed as$\sigma/\sqrt{N}$ where σ is the standard deviation and N is the total number of individual eddy realization at each weekly time step. Time series were smoothed in time prior to plotting with a filter half-power cutoff equivalent to a 21-day running mean.

composite averaged CHL'' and SLA in meanders (Fig. 7c and e) and eddies (Fig. 7d and f). Although the magnitude of CHL'' is larger in the simulations, likely a result of the larger variance of CHL in the simulations (Fig. 2e and h), it is quite remarkable how well the simulations reproduce the observed geographical structure of composite-averaged CHL''.

5.3. The time evolution of CHL in eddies and meanders

In the previous section, it was observed that the spatial structure of CHL'' composite averages may be attributable to multiple mesoscale physical/biological mechanisms. In this section, we evaluate the temporal evolution of CMS-centric CHL'' and ΔCHL' to help distinguish the influence of individual mechanisms.

Water with low CHL is entrained and transported eastward in the interiors of anticyclonic meanders during formation, as evidenced by negative (positive) CHL'' during the first 9 weeks of the lifetimes of anticyclonic (cyclonic) meanders (Fig. 8a). Note that the mean and variance of CHL (and associated normalizations of CHL' and CHL'') are substantially different in the models and observations (Fig. 2). As a result, the magnitudes of the composite-averaged time series cannot be compared; instead focus is placed on trends in these time series. Significant differences in eddy-centric CHL'' are a result of cyclonic and anticyclonic GS meanders containing slope and Sargasso Sea water, respectively. The southward displacement of slope water with elevated CHL in cyclonic meanders results in positive CHL''. On the other hand, the northward transport of Sargasso Sea water with low CHL in anticyclonic meanders results in negative CHL''. These significant differences in initial CHL'' are reproduced in both simulations (Fig. 8c and e). No significant temporal trends are generated in CHL following the formation of observed anticyclonic GS meanders, as assessed in the composite average time series of ΔCHL' (Fig. 8b). Significant changes in ΔCHL' are only generated during week 1 in observed cyclonic meanders (Fig. 8b), which are reproduced in both simulations (blue curve in Fig. 8d and f).

The temporal evolution of CHL in westward propagating eddies suggest that anticyclonic eddies entrain and trap low CHL water and cyclonic eddies trap water with elevated CHL, as evidence by positive (negative) CHL'' throughout the first 17 weeks of the lifetimes of cyclonic (anticyclonic) eddies (Fig. 9a, c and e). Following the formation of anticyclonic GS eddies, ΔCHL' exhibits a significant positive trend[2] (Fig. 9b).

An early analysis of individual satellite images of ocean color revealed that streamers of elevated CHL are entrained into the cores of warm-core rings (Brown et al., 1985). In addition, the work of Olson (1986) suggests that the lateral entrainment of water with elevated CHL into a warm-core ring would result in a positive trend in ΔCHL'. This lateral entrainment of elevated CHL by streamers is not present in eddy-centric composites, perhaps because the orientation and azimuthal position of the streamers vary relative to the eddy, thereby

---

[2] The trends are considered significant when the standard error of the composite averaged values do not encompass zero.

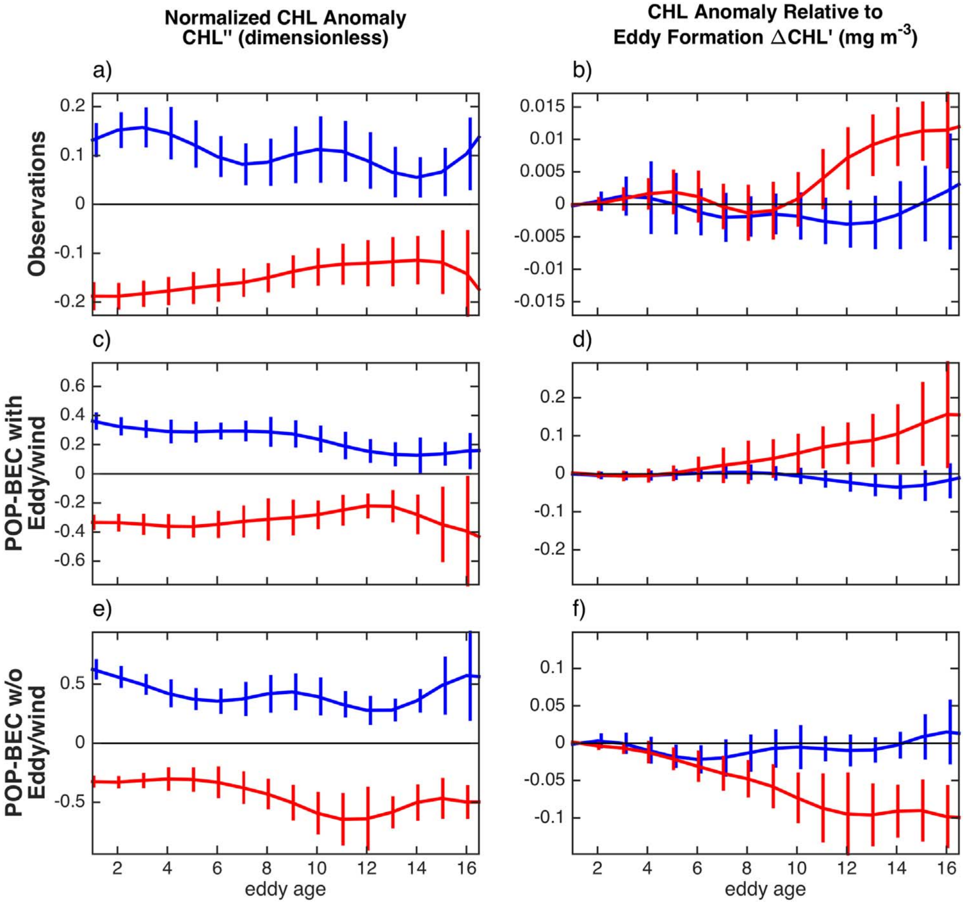

Fig. 9. Same as Fig. 8, except for westward propagating mesoscale eddies.

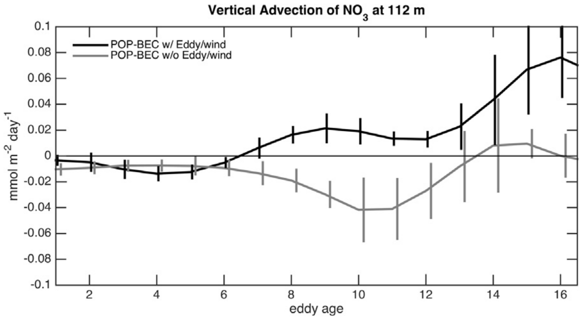

Fig. 10. Nutrient supply in anticyclones in the simulations with and without eddy/wind interaction, as indicated by composite average time series of vertical advection of NO_3 through the base of the euphotic zone (taken to be 112 m) within a radial distance of $0.5L_s$ of the eddies' SLA extremum.

causing them to be averaged out. Curiously, eddy-induced Ekman upwelling is expected to impede the lateral entrainment of CHL into anticyclones as a result of a net divergence in the Ekman layer inside of the eddy. How these two processes interact is an important avenue for future research.

In the simulation including eddy-induced Ekman pumping, a significant positive trend is observed in the interiors of anticyclonic eddies, albeit an order of magnitude larger than observed (Fig. 9d). This may be a result of overestimation of nutrient limitation in the model (see Section 4).The simulation without eddy-induced Ekman pumping, however, generates a negative trend in anticyclonic ΔCHL' (Fig. 9f), opposite to what is observed (Fig. 9b). Although the magnitude of the response to eddy-induced Ekman pumping is overestimated in the model, the fact that the model run without eddy-induced Ekman pumping produces a trend of the opposite sign suggests this mechanism may be generating the observed positive trend in ΔCHL' in GS anticyclones. It is interesting to note that the magnitude of ΔCHL' in the simulations is significantly larger than observed, which is consistent with the overestimation of nutrient limitation in the model during the summer (see Section 4).

6. Vertical nitrate fluxes in simulated Gulf Stream anticyclones

During the formation of anticyclonic GS eddies, water from the Sargasso Sea, characterized by low CHL and nutrients, is entrained from the south and subsequently trapped in the interiors of anticyclones, resulting in negative CHL'' (Fig. 7b, d and f and Fig. 9a, c and e). Following formation, a significant difference in the vertical advection of NO_3 into the euphotic zone exists between anticyclones in the two different simulations. In the model with eddy-induced Ekman pumping, significant upward advection of NO_3 occurs after week 7 (Fig. 10). In the interiors of the same anticyclones, ΔCHL' begins to become positive at week 6, however the positive trend is not significant until week 11 (Fig. 9d). This suggest that the upwelling of NO_3 has to persist for approximately 20 days before a significant positive trend in ΔCHL' ensues.

The simulation without eddy-induced Ekman pumping generates a net downwelling of NO_3 during the first 17 weeks of the lifetimes of anticyclonic eddies (Fig. 10). The difference in the sign of vertical advection of NO_3 and ΔCHL' between the two simulations, in conjunction with the observed positive trend in ΔCHL' in GS anticyclones suggest that the observed increase in CHL following the formation of GS anticyclones is possibly a result of eddy-induced Ekman upwelling of NO_3.

7. Discussion and conclusions

Gulf Stream eddies and meanders influence CHL *via* horizontal advection. Furthermore, the Ekman upwelling of nutrients in anticyclonic eddies, resulting from the influence of ocean surface currents on surface stress [Eq. (6)] increases CHL following eddy formation.

In the GS region, the cross correlation of CHL' and SLA is predominantly negative (Fig. 3a). The cross correlation in the interiors of CMS revealed that elevated CHL associated with cyclonic CMS is the primary contributor to the observed negative correlation (Fig. 3j). Composite averages of CHL'' in GS meanders consist of elevated and suppressed CHL in cyclonic and anticyclonic meanders, respectively (Fig. 7a). The composite averages are consistent with previous observations that suggest CMS act to entrain and transport CHL.

The composite-averaged CHL'' in GS eddies is similar to GS meanders: elevated and suppressed CHL'' in cyclones and anticyclones, respectively (Fig. 7b). Following formation, CHL within anticyclonic GS eddies increases, generating a significant positive trend in ΔCHL' (Fig. 9b). Comparison of the solutions of the coupled POP-BEC simulations with different surface forcing reveals that the inclusions of eddy-induced Ekman pumping generates a similar positive trend in ΔCHL' (Fig. 9d), whereas the solution without the surface current correction to the surface stress (and thus without eddy-induced Ekman pumping) gives rise to a negative trend in ΔCHL' (Fig. 9f). Analysis of the vertical advection of NO_3 in the cores of simulated GS anticyclones suggests that the eddy-induced Ekman upwelling of NO_3 (Fig. 10) is a likely mechanism generating the observed positive trend in ΔCHL'.

Upwelling occurring during the intensification of cyclonic eddies is expected to generate enhanced CHL'' at their cores. Although an increase in CHL'' and ΔCHL' in cyclones is observed during weeks 1–4, this trend is not significant (Fig. 9a and b). In contrast, Gaube et al. (2014) showed significant enhancement of CHL'' during the first 5 weeks of the lifetimes of cyclonic features in the Gulf Stream region, which they suggest could be a result of upwelling during eddy intensification. Differences in the evolution of CHL in cyclones between these two studies are not surprising as there are three significant distinctions in the methods used in the two studies: (1) The Gaube et al. (2014) analysis included all CMS in a rectangular region larger than the region considered here, resulting in the inclusion of open-ocean eddies that might not have originated in the GS region. (2) The current analysis is limited to the 5.5-year time period January 2000 through July 2005 whereas Gaube et al. (2014) analyzed observations during the 9 year period January 2001 through November 2009. (3) The current analysis isolates the effects of GS eddies and meanders on CHL, whereas Gaube et al. (2014) considers all CMS to be eddies. Interestingly, there is a modest increase in ΔCHL' during the first few weeks after the formation of cyclonic meanders (Fig. 8b), which may have contributed to the Gaube et al. (2014) finding of increasing CHL in cyclonic features.

It is important to note that we do not consider the impact of grazing and mortality of phytoplankton on observed CHL variability in eddies and meanders. Earlier work investigating the importance of grazing in warm core rings found significant lateral exchange between the grazer population inside and outside of the ring (Davis and Wiebe, 1985; Wiebe et al., 1985; Olson, 1986), suggesting that the grazing community varies as an eddy propagates.

In addition, climatologies of nutrient concentrations indicate that at times, phytoplankton growth may not be limited by nutrients (Conkright et al., 2002, and Fig. 4). Analysis of the eddy-centric composites of surface macro-nutrient (NO_3, NH_4, PO_4) concentrations in the simulations indicate that on average, both NO_3 and NH_4 are below their respective half-saturation constants for uptake by diatoms in eddies of both polarities (Table 2). This suggests that nitrogen is indeed limiting for diatoms in an average sense. Furthermore, our analysis of surface NO_3 in Section 4 concluded that over much of the study region, NO_3 is nearly zero both in summer and winter (Fig. 4) and eddy-centric composites of CHL" computed separately in summer and winter revealed very little differences in both spatial structure and magnitude (not shown). Small phytoplankton, however, do not appear to be limited by NO_3 or NH_4 in eddies (Table 2). The surface concentration of PO_4 does not appear to be limiting phytoplankton growth in Gulf Stream eddies. It is important to note, however, that the half saturation constant for uptake can be substantially larger than for growth. Alas, such complexity is rarely if ever included in three-dimensional biogeochemical models, and it is not part of the model used in this study.

Both top-down (grazing) and seasonal alleviation of nutrient limitation could result in temporal trends in eddy-centric CHL. However, without *in situ* estimates of vertical and horizontal fluxes of nutrients and grazers in evolving GS eddies and meanders, the conclusions drawn from the simulations presented herein cannot be confirmed. Repeat occupations of evolving GS eddies and meanders (The Ring Group, 1981; Joyce, 1985; Wiebe and McDougall, 1986; Wiebe and Joyce, 1992), including studies of the grazer community and tracer release experiments to constrain fluxes [*e.g.* Ledwell et al. (2008)], could be used to test the model-based conclusions presented here.

The study presented here details the analysis of hundreds of Gulf Stream eddies and meanders as observed by satellites and simulated in an eddy-resolving, coupled physical/biological model. We present the mean influence of eddies and meanders on CHL and conclude that the trapping of CHL during CMS formation is the primary mechanism contributing to observed negative correlation of SLA and CHL', which is consistent with prior studies based on synoptic realizations. Following the formation of anticyclonic eddies, the influence of the rotating eddy currents on the surface stress drives Ekman upwelling of nutrients into anticyclones, resulting in an observed positive trend in ΔCHL'. This mechanism has been observed in the central North Atlantic (Martin and Richards, 2001), Sargasso Sea (McGillicuddy et al., 2007) and the South Indian Ocean (Gaube et al., 2013). By itself, eddy-induced Ekman pumping is expected to result in positive correlation between SLA and CHL'. The observed negative correlation in the GS region suggests that the trapping of CHL during CMS formation tends to overshadow the effect of eddy-induced Ekman pumping. The finding of this study that multiple mesoscale physical/biological processes are active in GS eddies underscores the importance of the concurrent analysis of satellite and *in situ* observations with eddy-resolving, coupled physical/biological simulations to enable the influence of individual mechanisms to be quantified.

Acknowledgments

We thank Collecte Localis Satellites, AVISO (http://www.aviso.oceanobs.com) for the SLA observations, NASA MEaSUREs Ocean Color Product Evaluation Project (ftp://ftp.oceancolor.ucsb.edu/) for the ocean color observations and Larry Anderson for carrying out the model runs. The comments and suggestions of seven anonymous reviewers and five associated editors were greatly appreciated and resulted in considerable improvements to the manuscript. This work was funded by NASA, grant number NNX13AE47G grants OCE-1048897 and OCE-1558960 NSF, and a Postdoctoral Scholarship awarded to Peter Gaube from the Woods Hole Oceanographic Institution.

Appendix A. Supplementary material

Supplementary data associated with this article can be found in the online version at http://dx.doi.org/10.1016/j.dsr.2017.02.006.

References

Anderson, L.A., McGillicuddy, D.J., Maltrud, M.E., Lima, I.D., Doney, S.C., 2011. Impact of eddy-wind interaction on eddy demographics and phytoplankton community structure in a model of the North Atlantic Ocean. Dyn. Atmos. Oceans 52, 80–94.

Behrenfeld, M.J., Halsey, K.H., Milligan, A.J., 2008. Evolved physiological responses of phytoplankton to their integrated growth environment. Philos. Trans. R. Soc. B: Biol. Sci. 363 (1504), 2687–2703.

Bower, A.S., 1991. A simple kinematic mechanism for mixing fluid parcels across a meandering jet. J. Phys. Oceanogr. 21 (1), 173–180.

Boyd, S.H., Wiebe, P.H., Backus, R.H., Craddock, J.E., Daher, M.A., 1986. Biomass of the micronekton in Gulf Stream ring 82-B and environs: changes with time. Deep Sea Res. 33 (11), 1885–1905.

Boyer, T., Stephens, C., Antonov, J., Conkright, M., Locarnini, R., O'Brien, T., Garcia, H., 2002. World Ocean Atlas 2001. Salinity 2.

Brown, O., Evans, R., Brown, J., Gordon, H., Smith, R., Baker, K., 1985. Phytoplankton blooming off the US east coast: a satellite description. Science 229 (4709), 163–167.

Bryan, F.O., Hecht, M.W., Smith, R.D., 2007. Resolution convergence and sensitivity studies with North Atlantic circulation models. Part I: the western boundary current system. Ocean Model. 16 (3), 141–159.

Chelton, D.B., Gaube, P., Schlax, M.G., Early, J.J., Samelson, R.M., 2011a. The influence of nonlinear mesoscale eddies on Near-surface oceanic chlorophyll. Science 334 (6054), 328–332.

Chelton, D.B., Schlax, M.G., Samelson, R.M., 2011b. Global observations of nonlinear mesoscale eddies. Prog. Oceanogr. 91 (2), 167–216.

Chelton, D.B., Schlax, M.G., Samelson, R.M., de Szoeke, R.A., 2007. Global observations of large oceanic eddies. Geophys. Res. Lett. 34 (15).

Conkright, M., Garcia, H., O'Brien, T., Locarnini, R., Boyer, T., Stephens, C., Antonov, J., 2002. World Ocean Atlas 2001. Nutrients 4.

Craddock, J.E., Backus, R.H., Daher, M.A., 1992. Vertical distribution and species composition of midwater fishes in warm-core Gulf Stream meander/ring 82-H. Deep Sea Res. 39, S203–S218.

Davis, C.S., Wiebe, P.H., 1985. Macrozooplankton biomass in a warm-core Gulf Stream ring: time series changes in size structure, taxonomic composition, and vertical distribution. J. Geophys. Res.: Oceans 90 (C5), 8871–8884.

Dewar, W.K., Flierl, G.R., 1987. Some effects of the wind on rings. J. Phys. Oceanogr. 17 (10), 1653–1667.

Ducet, N., Le Traon, P., Reverdin, G., 2000. Global high-resolution mapping of ocean circulation from TOPEX/Poseidon and ERS-1 and-2. J. Geophys. Res. - Oceans 105 (C8), 19477–19498.

Ducklow, H., 1986. Bacterial biomass in warm-core Gulf Stream ring 82-B: mesoscale distributions, temporal changes and production. Deep Sea Res. 33 (11), 1789–1812.

Dufois, F., Hardman-Mountford, N.J., Greenwood, J., Richardson, A.J., Feng, M., Herbette, S., Matear, R., 2014. Impact of eddies on surface chlorophyll in the south indian ocean. J. Geophys. Res.: Oceans 119 (11), 8061–8077.

Eden, C., Dietze, H., 2009. Effects of mesoscale eddy/wind interactions on biological new production and eddy kinetic energy. J. Geophys. Res.: Oceans 114, (C05023).

Falkowski, P.G., LaRoche, J., 1991. Acclimation to spectral irradiance in algae. J. Phycol. 27 (1), 8–14.

Flierl, G.R., 1981. Particle motions in large-amplitude wave fields. Geophys. Astrophys. Fluid Dyn. 18 (1–2), 39–74.

Flierl, G.R., Davis, C.S., 1993. Biological effects of Gulf Stream meandering. J. Mar. Res. 51 (3), 529–560.

Fox, M.F., Bates, P.P., Kester, D.R., 1984. Nutrient data for Warm Core Ring 82-B from R/V Knorr Cruise 93. Thechnical Report. University of Rhode Island, Graduate School of Oceanography.

Franks, P.J.S., Wroblewski, J., Flierl, G.R., 1986. Prediction of phytoplankton growth in response to the frictional decay of a warm-core ring. J. Geophys. Res. 91 (C6), 7603–7610.

Fuglister, F.C., 1963. Gulf Stream '60. Prog. Oceanogr. 1, 265–373.

Fuglister, F.C., 1972. Cyclonic rings formed by the Gulf Stream 1965–66. In: Gordon, A.L. (Ed.), Studies in Physical Oceanography—A Tribute to Georg Wüst on His 80th Birthday. Gordon and Breach.

Garcia, H., Locarnini, R., Boyer, T., Antonov, J., Baranova, O., Zweng, M., Reagan, J., Johnson, D., 2014. World Ocean Atlas 2013, volume 4: Dissolved inorganic nutrients (phosphate, nitrate, silicate). NOAA Atlas NESDIS 76, 25.

García-Moliner, G., Yoder, J.A., 1994. Variability in pigment concentration in warm-core rings as determined by coastal zone color scanner satellite imagery from the Mid-Atlantic Bight. J. Geophys. Res.: Oceans 99 (C7), 14277–14290.

Garver, S.A., Siegel, D.A., 1997. Inherent optical property inverison of ocean color spectra and its biogeochemical interpertation: I. Time series from the Sargasso Sea. J. Geophys. Res.: Oceans 102, 18607–18625.

Gaube, P., 2012. Satellite Observations of the Influence of Mesoscale Ocean Eddies on Near-Surface Temperature, Phytoplankton and Surface Stress, Oregon State University, 104 CEOAS Admin Bldg. Corvallis, OR 97331 USA.

Gaube, P., Chelton, D.B., Samelson, R.M., O'Neill, L.W., Schlax, M.G., 2015. Satellite observations of mesoscale eddy-induced Ekman Pumping. J. Phys. Oceanogr. 45, 104–132.

Gaube, P., Chelton, D.B., Strutton, P.G., Behrenfeld, M.J., 2013. Satellite observations of chlorophyll, phytoplankton biomass and Ekman pumping in nonlinear mesoscale eddies. J. Geophys. Res.: Oceans 118, 1–22.

Gaube, P., McGillicuddy, D.J., Jr, Chelton, D.B., Behrenfeld, M.J., Strutton, P.G., 2014. Regional variations in the influence of mesoscale eddies on Near-surface chlorophyll. J. Geophys. Res.: Oceans 119, 1–26.

Geider, R.J., 1987. Light and temperature dependence of the carbon to chlorophyll a ratio in microalgae and cyanobacteria: implications for physiology and growth of phytoplankton. New Phytol. 106 (1), 1–34.

Gordon, H., Clark, D., Brown, J., Brown, O., Evans, R., 1982. Satellite measurement of the phytoplankton pigment concentration in the surface waters of a warm core Gulf Stream Ring. J. Mar. Res. 40 (2), 491–502.

Hitchcock, G.L., Langdon, C., Smayda, T., 1985. Seasonal variations in the phytoplankton biomass and productivity of a warm-core Gulf Stream ring. Deep Sea Res. Part A. Oceanogr. Res. Pap. 32 (11), 1287–1300.

Hitchcock, G.L., Mariano, A.J., Rossby, T., 1993. Mesoscale pigment fields in the Gulf Stream: observations in a meander crest and trough. J. Geophys. Res.: Oceans (1978–2012) 98 (C5), 8425–8445.

Hutchinson, D.K., Hogg, A.M.C., Blundell, J.R., 2010. Southern Ocean response to relative velocity wind stress forcing. J. Phys. Oceanogr. 40 (2), 326–339.

Joyce, T.M., 1985. Gulf Stream warm-core ring collection: an introduction. J. Geophys. Res.: Oceans (1978–2012) 90 (C5), 8801–8802.

Kang, D., Curchitser, E.N., 2013. Gulf Stream eddy characteristics in a high-resolution ocean model. J. Geophys. Res.: Oceans 118 (9), 4474–4487.

Key, R.M., Kozyr, A., Sabine, C.L., Lee, K., Wanninkhof, R., Bullister, J.L., Feely, R.A., Millero, F.J., Mordy, C., Peng, T.H., 2004. A global ocean carbon climatology: results from Global Data Analysis Project (GLODAP). Glob. Biogeochem. Cycles 18 (4).

Large, W.G., Yeager, S.G., 2004. Diurnal to decadal global forcing for ocean and sea-ice models: The data sets and flux climatologies. NCAR Tech. Note p. 111.

Laws, E.A., Bannister, T., 1980. Nutrient-and light-limited growth of Thalassiosira fluviatilis in continuous culture, with implications for phytoplankton growth in the ocean. Limnol. Oceanogr. 25 (3), 457–473.

Ledwell, J.R., McGillicuddy Jr, D.J., Anderson, L.A., 2008. Nutrient flux into an intense deep chlorophyll layer in a mode-water eddy. Deep Sea Res. Part II: Top. Stud. Oceanogr. 55 (10–13), 1139–1160.

Lévy, M., Klein, P., Treguier, A.M., 2001. Impact of sub-mesoscale physics on production and subduction of phytoplankton in an oligotrophic regime. J. Mar. Res. 59 (4), 535–565.

Lévy, M., Mémery, L., Madec, G., 1998. The onset of a bloom after deep winter convection in the northwestern Mediterranean sea: mesoscale process study with a primitive equation model. J. Mar. Syst. 16 (1), 7–21.

Lévy, M., Mémery, L., Madec, G., 1999. The onset of the spring bloom in the MEDOC area: mesoscale spatial variability. Deep Sea Res. Part I: Oceanogr. Res. Pap. 46 (7), 1137–1160.

Lima, I.D., Olson, D.B., Doney, S.C., 2002. Biological response to frontal dynamics and mesoscale variability in oligotrophic environments: biological production and community structure. J. Geophys. Res.: Oceans 107 (C8), (25-21-25-21).

Locarnini, R., Mishonov, A., Antonov, J., Boyer, T., Garcia, H., Baranova, O., Zweng, M., Paver, C., Reagan, J., Johnson, D., 2013. World Ocean Atlas 2013, vol. 1. A. Mishonov Technical Ed.

Locarnini, R.A., Mishonov, A.V., Antonov, J.I., Boyer, T.P., Garcia, H.E., Levitus, S., 2006. World Ocean Atlas 2005 Volume 1: Temperature 1. NOAA Atlas NESDIS 51. U.S. Government Printing Office, Washington, DC.

Maritorena, S., Siegel, D.A., Peterson, R., 2002. Optimization of a semianalytical ocean color model for global-scale applications. Appl. Opt. 41 (15), 2705–2714.

Martin, A.P., Richards, K.J., 2001. Mechanisms for vertical nutrient transport within a North Atlantic mesoscale eddy. Deep Sea Res. II 48 (4–5), 757–773.

McGillicuddy, D., Anderson, L., Doney, S., Maltrud, M., 2003. Eddy-driven sources and sinks of nutrients in the upper ocean: results from a 0.1 resolution model of the North Atlantic. Glob. Biogeochem. Cycles 17 (2).

McGillicuddy, D., Kosnyrev, V., Ryan, J., Yoder, J., 2001. Covariation of mesoscale ocean color and sea-surface temperature patterns in the Sargasso Sea. Deep Sea Res. Part II: Top. Stud. Oceanogr. 48 (8), 1823–1836.

McGillicuddy, D.J., Anderson, L.A., Bates, N.R., Bibby, T., Buesseler, K.O., Carlson, C.A., Davis, C.S., Ewart, C., Falkowski, P.G., Goldthwait, S.A., et al., 2007. Eddy/wind interactions stimulate extraordinary Mid-Ocean Plankton Blooms. Science 316 (5827), 1021.

McGillicuddy, D.J., Jr, 2015. Formation of intrathermocline lenses by eddy–wind interaction. J. Phys. Oceanogr. 45 (2), 606–612.

McWilliams, J.C., Flierl, G.R., 1979. On the evolution of isolated, nonlinear vortices. J. Phys. Oceanogr. 9 (6), 1155–1182.

Moore, J.K., Doney, S.C., 2007. Iron availability limits the ocean nitrogen inventory stabilizing feedbacks between marine denitrification and nitrogen fixation. Glob. Biogeochem. Cycles, 21, (GB2001).

Moore, J.K., Doney, S.C., Kleypas, J.C., Glover, D.M., Fung, I.Y., 2002. An intermediate complexity marine ecosystem model for the global domain. Deep-Sea Res. II 49, 403–462.

Moore, J.K., Doney, S.C., Lindsay, K., 2004. Upper ocean ecosystem dynamics and iron cycling in a global three-dimensional model. Glob. Biogeochem. Cycles 18, (GB4028).

Moore, J.K., Doney, S.C., Lindsay, K., Mahowald, N., Michaels, A.F., 2006. Nitrogen fixation amplifies the ocean biogeochemical response to decadal timescale variations in mineral dust deposition. Tellus 58B, 560–572.

Nelson, D.M., McCarthy, J.J., Joyce, T.M., Ducklow, H.W., 1989. Enhanced near-surface nutrient availability and new production resulting from the frictional decay of a Gulf Stream warm-core ring. Deep Sea Res. Part A. Oceanogr. Res. Pap. 36 (5), 705–714.

Olson, D.B., 1986. Lateral exchange within Gulf Stream warm-core ring surface layers. Deep Sea Res. 33 (11), 1691–1704.

Olson, D.B., Backus, R.H., 1985. The concentrating of organisms at fronts: a cold-water fish and a warm-core Gulf Stream ring. J. Mar. Res. 43 (1), 113–137.

Olson, D.B., Hitchcock, G., Mariano, A., Ashjian, C., Peng, G., Nero, R., Podesta, G., 1994. Life on the edge: marine life and fronts. Oceanography 7 (2), 52–60.

Olson, E.M., McGillicuddy, D.J., Flierl, G.R., Davis, C.S., Dyhrman, S.T., Waterbury, J.B.,

2015. Mesoscale eddies and Trichodesmium spp. distributions in the southwestern North Atlantic. J. Geophys. Res.: Oceans.

Pacanowski, R.C., Philander, S.G.H., 1981. Parameterization of vertical mixing in numerical models of tropical oceans. J. Phys. Oceanogr. 11 (11), 1443–1451.

Pascual, A., Ruiz, S., Buongiorno Nardelli, B., Guinehut, S., Iudicone, D., Tintoré, J., 2015. Net primary production in the Gulf Stream sustained by quasi-geostrophic vertical exchanges. Geophys. Res. Lett. 42, 441–449.

Pingree, R., Holligan, P., Mardell, G., 1979. Phytoplankton growth and cyclonic eddies. Science 278, 245–247.

Richardson, P.L., 1980. Gulf Stream ring trajectories. J. Phys. Oceanogr. 10 (1), 90–104.

Ryan, J., Yoder, J., Townsend, D., 2001. Influence of a Gulf Stream warm-core ring on water mass and chlorophyll distributions along the southern flank of Georges Bank. Deep Sea Res. Part II: Top. Stud. Oceanogr. 48 (1), 159–178.

Siegel, D., Maritorena, S., Nelson, N., Hansell, D., Lorenzi-Kayser, M., 2002. Global distribution and dynamics of colored dissolved and detrital organic materials. J. Geophys. Res.: Oceans 107 (C12), 3228.

Smith, R., Baker, K., 1985. Spatial and temporal patterns in pigment biomass in Gulf Stream warm-core ring 82B and its environs. J. Geophys. Res.: Oceans 90 (C5), 8859–8870.

Spall, S., Richards, K., 2000. A numerical model of mesoscale frontal instabilities and plankton dynamics—I. Model formulation and initial experiments. Deep Sea Res. Part I: Oceanogr. Res. Pap. 47 (7), 1261–1301.

Stephens, C., Antonov, J., Boyer, T., Conkright, M., Locarnini, R., O'Brien, T., Garcia, H., 2002. World Ocean Atlas 2001. Temperature 1.

The Ring Group, 1981. Gulf stream cold-core rings: their physics, chemistry, and biology. Science 212 (4499), 1091.

Von Storch, H., Zwiers, F.W., 1999. Statistical Analysis in Climate Research. Cambridge University Press, New York, NY, USA.

Wiebe, P.H., Flierl, G.R., Davis, C.S., Barber, V., Boyd, S.H., 1985. Macrozooplankton biomass in Gulf Stream warm-core rings: spatial distribution and temporal changes. J. Geophys. Res.: Oceans (1978–2012) 90 (C5), 8885–8901.

Wiebe, P.H., Hulburt, E.M., Carpenter, E.J., E Jahn, A., Knapp, G.P., Boyd, S.H., Ortner, P.B., Cox, J.L., 1976. Gulf Stream cold core rings: large-scale interaction sites for open ocean plankton communities. Deep Sea Res. Oceanogr. Abstr., 695–710.

Wiebe, P.H., Joyce, T.M., 1992. Introduction to interdisciplinary studies of Kuroshio and Gulf Stream rings. Deep Sea Res. 39, 5–6.

Wiebe, P.H., McDougall, T., 1986. Warm-core rings: studies of their physics, chemistry and biology. Deep-Sea Res. 33 (11–12).

Woods, J.D., 1988. Mesoscale upwelling and primary production. In: Rothschild, B.J. (Ed.), Toward a Theory on Biological-Physical Interactions in the World Ocean. D. Reidel, Dordrecht, 7–23.